Order Number 9123459

Cesium atomic resonance filter

Batdorf, Brian James, Ph.D.
The University of Arizona, 1991

U·M·I
300 N. Zeeb Rd.
Ann Arbor, MI 48106

Cesium Atomic Resonance Filter

by

Brian James Batdorf

A Dissertation Submitted to the Faculty of the

COMMITTEE on OPTICAL SCIENCES (Graduate)

In Partial Fulfillment of the Requirements
For the Degree of

DOCTOR OF PHILOSOPHY

In the Graduate College

THE UNIVERSITY OF ARIZONA

1 9 9 1

THE UNIVERSITY OF ARIZONA
GRADUATE COLLEGE

As members of the Final Examination Committee, we certify that we have read the dissertation prepared by Brian James Batdorf

entitled Cesium Atomic Resonance Filter

and recommend that it be accepted as fulfilling the dissertation requirement for the Degree of Doctor of Philosophy.

Dr. H. Angus Macleod	February 12, 1991 Date
Dr. Michael R. Jacobson	February 12, 1991 Date
Dr. Richard L. Shoemaker	February 12, 1991 Date
	Date
	Date

Final approval and acceptance of this dissertation is contingent upon the candidate's submission of the final copy of the dissertation to the Graduate College.

I hereby certify that I have read this dissertation prepared under my direction and recommend that it be accepted as fulfilling the dissertation requirement.

Dissertation Director Dr. H. Angus Macleod	February 12, 1991 Date

STATEMENT BY AUTHOR

This dissertation has been submitted in partial fulfillment of requirements for an advanced degree at The University of Arizona and is deposited in the University Library to be made available to borrowers under the rules of the Library.

SIGNED: Brian James Baldorf

Acknowledgements

I would like to thank, or perhaps more appropriately dedicate this work to the many people who have led me in the right direction in the course of my studies. Angus Macleod, my advisor, was a major influence in my progress well before I was a student of his. Unfortuately, the thin film work done on this project to turn this academic exercise into a useful device was interesting, but not pursued far enough to fall under the heading of new research and therefore does not appear in this manuscript. It was challenging none the less. Mike Jacobson deserves many thanks for his almost endless patience in reading revisions of this dissertation and for his practical advice. He and Bertrand Bovard were always willing to discuss problems and, more useful to the student, provide direction, as was Richard Shoemaker, the final member of my committee. Also leading the list of people instrumental to the existence and success of this work was Robert Lintell, who, through Science Applications International Corp., supported me with a research assistantship and provided the connection between the computer modeling and filter design at the University of Arizona and the experimental work performed by SAIC.

Table of Contents

List of Illustrations

List of Tables

ABSTRACT

An atomic resonance filter (ARF), composed of a cell containing an absorbing gas and two interference/absorption filter stacks, is designed to be both wide angle and ultra-narrowband. The bandwidth of this filter, in the range of 1-10mÅ, is determined by the absorption linewidth of the absorbing gas. Light entering the ARF within this bandwidth excites the gas to a highly excited state, and the fluorescence cascade back to the ground state emerges from the gas cell as the detected signal. The interference/absorption filter stacks insure that light not interacting with the gas does not pass through the ARF. The ARF is necessarily wide-angle due to the isotropic absorption properties of the gas.

This dissertation models the processes involved in atomic absorption to determine the performance of an ARF that uses cesium as the absorbing gas. This model uses the Voigt absorption profile to obtain a correlation between the frequency of the traveling photon and the velocity of the absorbing atom. Results of computer simulations based on this model are presented along with experimental measurements.

The ARF characteristics of importance include its efficiency and the temporal response of the filter. These characteristics are determined as a function of temperature and the input photon frequency. The effect of an additional buffer gas, which is included to decrease the ARF response time is investigated.

Section 1: Symbol List and Conversion Factors

N	atomic density [atoms/liter]	
T	temperature [°K]	
T_r	cell reservoir temperature	
P	pressure [torr]	
k_B	Boltzmann's constant	$k_B = 1.38 \cdot 10^{-23}$ J/°K $= 8.6 \cdot 10^{-5}$ eV/°K
h	Planck's constant	$h = 6.626 \cdot 10^{-34}$ J·sec $= 6.58 \cdot 10^{-16}$ eV·sec
W	evaporation rate of a liquid	
l,L	azimuthal quantum number of a single electron, all electrons	
m,M	magnetic quantum number of a single electron, all electrons	
s,S	spin quantum number	
I	nuclear spin quantum number	
j,J	total angular momentum of electron (orbit + spin)	$j=l+s, J=L+S$
F	total angular momentum of the atom (nucleus + e^-)	$F=I+J$
e	electron charge $1.6*10^{-19}$ C	
r	displacement vector	
Ψ	eigenfunction, or electron wave function	

ν	photon frequency
ν_o	photon frequency in atom's reference frame
$\Delta\nu$	frequency offset, or frequency as measured from line center
v_x	atom's projected velocity along photon's trajectory
m_{Cs}	mass of cesium atom

Conversion Factors

at 455nm: 1 mÅ = 0.145 GHz = 0.0048 cm^{-1}

at 850nm: 1 mÅ = 0.0415 GHz = 0.00138 cm^{-1}

Section 2: Introduction

Optical filters take many forms depending on the wavelengths involved and the temporal nature of both the desired signal and background noise. The specific problem that this dissertation addresses is the detection of a weak narrowband signal that is present amid a strong, wide-band background. The filter employed for this task must be insensitive to small changes in temperature, have high rejection out-of-band, high transmission in-band, and perform over extremely wide angles (up to $\pm$ 90°). The filter discussed here, the atomic resonance filter (ARF), has the high rejection/wide angle properties of absorption filters *and* the narrow bandwidth property of interference filters. To realize this potential conventional interference and absorption filters are added as pre- and post-filters to the primary component, a gas filled fluorescent cell.

ARFs are intrinsically wide-angle, since they are based on the atomic absorption of photons, which is an isotropic process. The atomic transition of the absorbing gas determines the ultranarrow bandwidths of this filter (1-10 mÅ) and its ultra-high value of Q[1] ($Q \equiv \Delta\lambda/\lambda \sim 10^6$). Only photons which fall very close to the transition wavelength are detected, so that these filters are well suited for operation against a continuum background. In addition to these characteristics, ARFs tend to have low intrinsic noise, high efficiencies, and fast response times. Owing to their unique properties, ARFs have successfully supported laser communications[2], underwater communications[3], lidar[4], and meteorology[5,6]. The Cs ARF in particular is a good

candidate for underwater communications since its excitation wavelength falls within the blue-green region where water has a minimum in absorption.

Figure 2.1 shows schematically how the absorption and interference filters are integral parts of the ARF system. They combine to create an effective edge filter that has a sharp cut-off wavelength and no side-bands. The atomic vapor cell is sandwiched between two such edge filters, one short-wave pass (SWP) and one long-wave pass (LWP) filter. These edge filters are designed to have non-overlapping spectral bandpasses, with the SWP filter on the input side and the LWP filter on the output side. The transmission characteristics of each element are presented in Figures 2.2a,b and c. The atomic vapor is transparent at all wavelengths except at the atomic transition wavelengths. Figures 2.2d,e,f and g plot the spectral intensity that passes each successive element. The small "blip" that is on top of the wide-band noise is the input signal. Since the edge filters have no common bandpass, light not interacting with the vapor does not pass through to the detector on the output side. However, light which interacts with the vapor, exciting it to a level well above the ground state, produces several fluorescence photons at longer wavelengths which do pass through the output LWP filter. It is this wavelength shifted light that is the output signal. It is important to note that the output signal, while being fundamentally linked to the input photon, originates from the radiative cascade from a highly excited atom. Therefore the ARF is unlike either an absorption or interference filter since imaging of the input signal source is not possible after filtering.

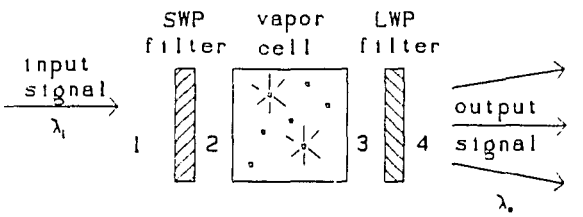

Figure 2.1. Atomic resonance filter design. (numbers are referenced in Figure 2.2.)

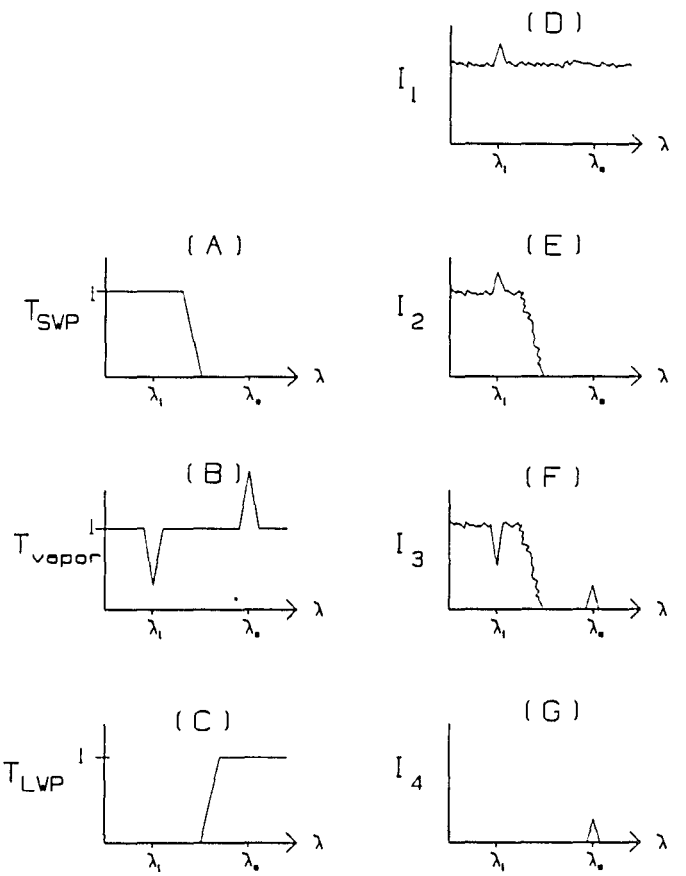

Figure 2.2. Wavelength response of ARFs. (A), (B) and (C) show the transmission characteristics of the individual elements. (D), (E), (F) and (G) show the spectral intensities at regions 1-4 as denoted in Figure 2.1. The small blip at λ_i is the input signal and the corresponding output signal appears at λ_o.

The process above describes the operation of a passive resonance filter. Passive filters operate with the absorbing gas in the ground state and are designated as ARFs in this dissertation. The output signal from a passive ARF always has a longer wavelength than the input signal. If the input wavelength is in the visible region as determined by other system parameters, such as the source or medium between transmitter and detector, then this wavelength shift could place the output signal well into the IR, where photon detectors are less responsive.

A filter that actually preceded the ARF[7] has a wavelength shift in the opposite sense, making it an ideal choice for the above problem. Called a laser excited optical filter (LEOF), it was first designed to upshift light frequencies from the IR to a the near-UV to increase the output from photo-multiplier tube (PMT) detectors, since PMTs are more efficient at shorter wavelengths. In contrast to ARFs, LEOFs are active filters, operating by signal absorption from a prepared, excited state. The operational difference between ARFs and LEOFs is diagrammed in Figure 2.3.

The elements that fluoresce in the atomic vapor cells have primarily been from groups IA (the alkali metals) and IIA (the alkaline earth metals) of the periodic table. These operate in a desirable wavelength region (the middle of the visible spectrum), have well-known spectra, are characterized by strong transitions and have high vapor pressures. The 532-536nm wavelength region has become especially popular due to the availability of well-behaved frequency-doubled laser sources. Doped Nd lasers (such

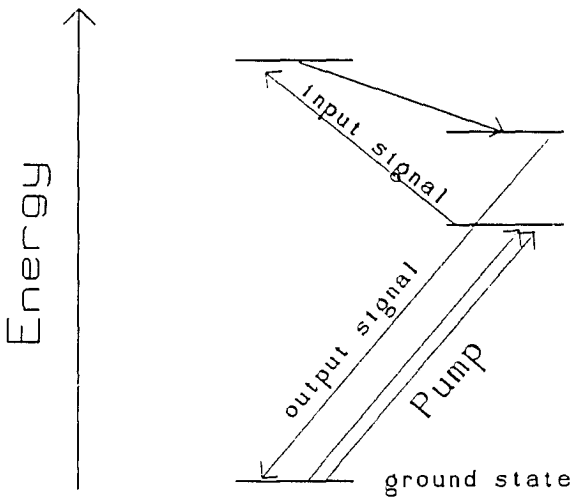

(A) LEOF energy level diagram.

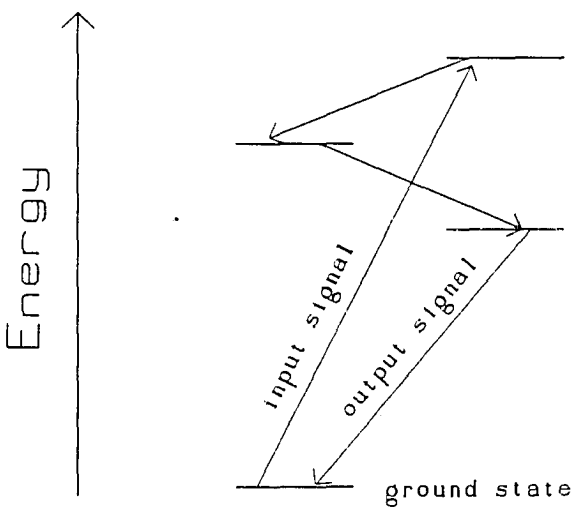

(B) ARF energy level diagram.

Figure 2.3. Comparison between the use of energy levels in LEOF and ARF designs.

as Nd:YAG, Nd:BEL, Nd:LNA and Nd:YALO) dominate in this arena since they are easily controlled by temperature-tuning and their output at about 1 μm can be frequency-doubled into the desired 532-536nm range. Table 2.1 and Table 2.2 show the specifications for several LEOF and ARF designs that have surfacedin the literature.

Table 2.1. LEOF examples and specifications

element	λ_{input} (nm)	λ_{output} (nm)	λ_{pump} (nm)	efficiency
Ca[8]	422.7	272	672	~95%
K[9]	532.3	404.5	769.8	~7%
Mg[10]	516,517,518			
Na[11]	1480	498	330	~50%
Rb[12]	532	420,359,323	795	
Th-Cs[13]				

Table 2.2. ARF examples and specifications[14]

element	λ_{input} (nm)	λ_{output} (nm)	efficiency
Cs	455, 459	852, 894	>95%
K	464.2	766, 770	~100%
Rb	516	780, 795	~100%
Rb	420	780, 795	~95%

The choice of which filter is best suited for a particular application depends on many factors. When the background is intense and wide-band, such as the solar reflectance from the Earth's surface, then the exact wavelength placement is crucial.

The solar spectrum outside the atmosphere has the overall shape of a 6000 °K blackbody except for emission dips known as the Fraunhofer lines. These lines are caused by the absorption of light by the atomic species that lie in the outer layer of the sun. There are twenty four strong lines[15] in the wavelength region from 400 to 760nm. These dips in the spectrum serve as natural, low background bands for narrowband optical communications. In fact, the Ca and Mg LEOFs are designed to take advantage of these bands. These filters have superior daylight performance because the solar background is only 2.4% and 7% of the calculated blackbody intensity at 422 and 518nm, respectively. The Ca vapor cell has the additional benefit of being devoid of hyperfine splitting (hfs). The hfs of energy levels is great enough in certain cases to create multiple fully resolved absorption lines where only one would exist otherwise. Since the absorption linewidth is generally wider than the signal width to start with, the others only serve to absorb more background radiation, whereby contributing to the noise and degrading performance.

A single absorption line has a width that depends on the natural, collisional and Doppler widths. The natural width is determined solely by the lifetime of the excited state. The collisional width contribution is caused by the interruptions in phase of the emitted radiation, caused by impact by a second atom, which broadens the spectral bandwidth. It is dependent on the pressures of all gas species present. The Doppler width is due to the Brownian motion of the absorbing atoms; it has a greater value for light atoms at high temperatures. As far as background rejection is concerned, a

narrow width absorption line has superior performance, assuming of course that the source is very narrow, controllable and stable.

However, the widening of the absorption line in the case of collision broadening is accompanied by an increase in the relaxation rate of the excited states, which is a desirable effect. Neon buffer gas served this function for the work presented here since, unlike helium, it does not easily diffuse through glass. The decrease in excited state lifetimes translates into a faster response time for the system. For a communications system, it is the response time that limits the information transmission rate.

A second effect, radiation trapping, also plays a role in determining the final response time. Radiation trapping occurs when a photon is absorbed and re-emitted many times as it traverses an absorbing medium. It is especially prominent for photons that are emitted in a transition to the ground state, since many surrounding atoms can readily absorb photons of this wavelength. Because many absorptions/re-emissions occur in this case, the response time is lengthened, resulting in an effect known as pulse stretching.

The ARF studied in this dissertation is based on the 455 and 459nm absorption lines of cesium, which is a candidate for a proposed communications system. It is a passive filter and the fluorescence signal appears at both 852 and 894nm. This ARF

is modeled by computer and verified by experimental data for several measurable parameters. The impetus for modeling this system is to create a tool for optimizing the filter efficiency and response time.

The modeling revolves around equations that are easily found in common laser spectroscopy texts by authors such as Seigman[16] and Milonni[17]. It involves the basic equations of natural, collisional and Doppler broadening. More advanced topics are also taken into hand, such as the line skewing and shifting that occurs with collisional broadening. Radiation trapping is easily observed in this system by its effect on pulse broadening and lineshape redistribution. The response time of an isolated Cs atom is about 0.3 μsec as determined by the radiative cascade from the excited state. However, under certain conditions, radiation trapping increases this to several microseconds as the output signal is more strongly absorbed than the input signal.

Modeling by numerical methods is the only realistic way of including the effects of all these processes. The performance of such a system is dependent on the physical parameters, such as temperature and pressure, as well as the engineering parameters, such as the spectral reflectivity of the containment walls enclosing the atomic vapor. The output variables of efficiency and response time are obtained as a function of temperature, gas pressure, and input signal parameters.

The overall goal of this work has three parts. The first part is model

verification. This takes the form of a comparison to published literature and two experiments, one that measures the 455nm light transmitted through the containment cell vs. temperature and the second which compares conversion efficiency vs. temperature. The second part finds the output variables for an ideal cell, one having perfect SWP and LWP filters. The third part investigates the properties of a gas slab without any containment walls. Radiation trapping alters the frequency distribution of light emitted from this slab; the amount of change depends on the thickness of the gas slab.

The sections of this dissertation are arranged and defined as follows.

Section 1: Symbols List

Section 2: Introduction This provides a brief description of the operation of an atomic resonance filter and gives examples cited in literature.

Section 3: Properties of Cesium This provides the published vapor pressure and density of Cs atoms as a function of temperature and the evaporation rate from the liquid state. Also included is the energy level diagram along with fine and hyperfine splitting explanations and constants.

Section 4: Lorentz Broadening This discusses the broadening associated with the natural lifetime and collisions.

Section 5: Doppler Broadening The effect of Brownian motion on the linewidth is reviewed.

Section 6: The Voigt Profile This spectral profile results when both Lorentzian and

Gaussian broadening are present. The convolution process is reviewed to express this line shape.

Section 7: Simulation of Atomic Absorption and Gas Kinetics The processes that occur as a photon travels through a gas are presented. The correlation between photon frequency and atom velocity is derived and supported by results seen in the literature.

Section 8: Model Verification and ARF Performance The results from experiment are shown along with simulation values for 455nm absorption and conversion efficiency vs. temperature.

Section 9: Radiation Trapping Both theory and simulation are presented to show how the emission lineshape of a volume of gas evolves as the gas layer thickness increases.

Section 10: Sources of Noise Included here are the effects of photoionization and collisional energy pooling.

Section 11: Discussion of Results and Conclusion

Appendix A: Production of numbers that obey desired probability laws is covered.

Section 3: Properties of Cesium

The properties of the atomic vapor are obtained using the constants found in this section. The first part deals with the liquid/gas transition, which is relevant to understanding situations in which Cs vapor is derived from an abundant liquid source. Both the rate of evaporation and the steady state vapor concentration are examined. The second part encompasses the spectroscopy of cesium vapor, including a brief description of the splitting of state energies.

Cesium Vapor Pressure and Density

The physics involved in atomic absorption of radiation of a gas hinge upon the temperature, T, and atomic density, N. If the vapor is derived from a liquid source so that equilibrium is established between the gas and liquid phases, then the vapor pressure and N are a function of T. The convention used hereon is that if this equilibrium condition exists, the chamber is overfilled, in which case the vapor is saturated; if only the gas phase exists then the chamber is underfilled. An experiment that uses an initially underfilled chamber is burdened by large uncertainties in the exact Cs density for several reasons. First, there is difficulty in accurately measuring the very small pressures involved. One must work below the saturation pressure, which is 1 μtorr of Cs vapor pressure at ambient temperatures. Second, the vapor density gradually decreases over time due to cesium's tendency to attack and combine with

residual gases and the chamber itself. And last, even if the chamber is initially underfilled, a change to lower temperatures rapidly causes saturation, at which point condensation occurs on the walls, reducing the vapor density and occluding the chamber walls. So, the usual method for maintaining a known vapor density is to attach a "cold" reservoir to the chamber that is filled with an excess of liquid cesium. For a stable reservoir temperature, the vapor pressure of atomic cesium reaches an equilibrium value[18] that is described by the following equation,

$$\log_{10}(p_{Cs})=8.22-\frac{4006}{T}-(6.02e-4)T-0.196\log_{10}(T) \qquad (3.1)$$

and is graphically represented in Figure 3.1 along with the pressure of diatomic Cs (Cs_2). Cs_2 is always present at equilibrium as a result of collisions between free Cs atoms. For temperatures in the neighborhood of 100°C the Cs vapor pressure is low enough so that the ideal gas law is valid.

$$P=Nk_BT \qquad (3.2)$$

Here P, N, k_B, and T, denote the pressure [torr], atom density [atoms/liter], Boltzmann's constant and temperature [°K] respectively. The number density then follows the simplified formula below.

$$density\left[\frac{atoms}{cm^3}\right] = 9.65\times10^{18}\ \frac{P[torr]}{T[^\circ K]} \qquad (3.3)$$

This is graphed in Figure 3.2. Before proceeding, one note should be made on the experiment with such an arrangement. The temperature of the relatively cool reservoir

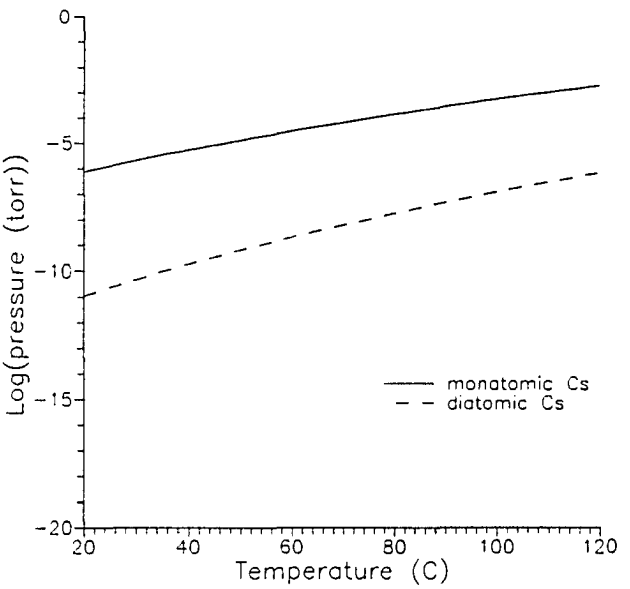

Figure 3.1. Pressure vs. temperature for monatomic and diatomic cesium.

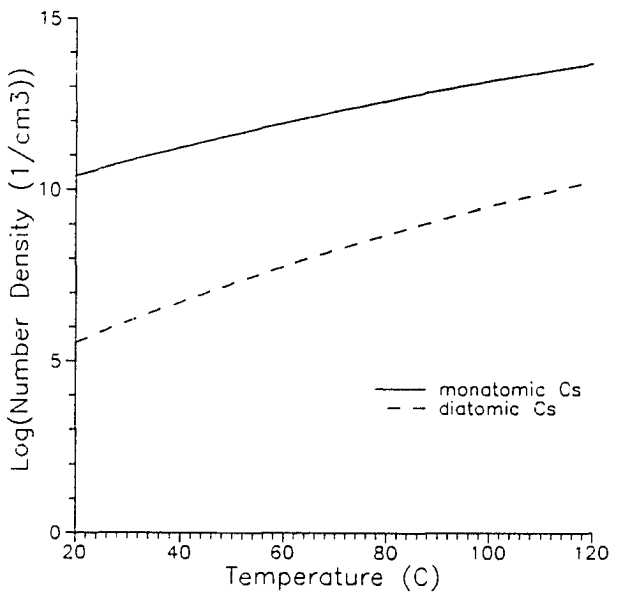

Figure 3.2. Density vs. temperature for monatomic and diatomic cesium.

determines N within the chamber. Since it is cooler than the other parts of the chamber, all evaporation and condensation will occur there. If the surface area of the reservoir is small in comparison with the total chamber surface area, then we can assume that the warmer temperature of the chamber is what determines the average atom velocities and the dynamics of the vapor.

Cesium Evaporation Rate

The relative surface areas are proportioned to validate this approximation. However, this slows the equilibration of atom density when the reservoir temperature changes, since all evaporation takes place over a small surface. The rate of evaporation (W) is given[19] by the expression below and is graphed in Figure 3.3.

$$\log_{10}\left(W\left[\frac{grams}{sec\cdot cm^2}\right]\right)=9.86-\frac{3.77\times10^3}{T}-\frac{1}{2}\log_{10}(T)-3.17 \qquad (3.4)$$

A simple calculation that assumes immediate mixing of the evaporated cesium gives very fast equilibration times which are an order of magnitude faster than those observed in the laboratory. Thus it is probable that other factors, such as the thermal transfer time across the reservoir walls and atomic diffusion time, are the dominant processes in establishing the equilibration time for our experiments.

Cesium Spectrum

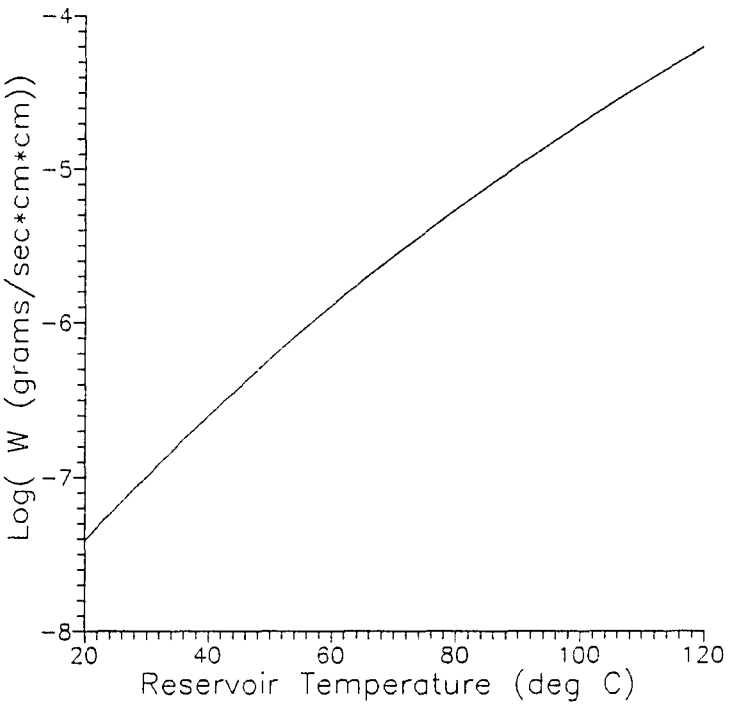

Figure 3.3. Rate of cesium evaporation (W) vs temperature.

The remainder of this section is devoted to the absorption (emission) spectrum of cesium. The splitting of energy levels and its effect on the final absorption lineshape are discussed. From this discussion, the reader will achieve qualitative insight into the relative magnitudes involved in fine and hyperfine spectroscopic structures.

The Schrödinger equation,

$$\nabla^2\Psi + v\Psi = i\frac{h}{2\pi}\frac{\partial\Psi}{\partial t} \quad , \tag{3.5}$$

is used to solve for the steady-state solutions for the electron wavefunction. The solutions, or eigenfunctions, are characterized by the quantum numbers n, l and m. n is the principal quantum number. l is the azimuthal quantum number and corresponds to the angular momentum of the electronic probability density function. m is the magnetic quantum number and defines the spatial orientation. In the absence of an external field, eigenfunctions that differ only in m have equal energy levels; this is called space degeneracy. The selection rules for dipole allowed transitions are

$$\Delta l = \pm 1 \qquad \Delta m = 0, \pm 1 \tag{3.6}$$

These must be followed to have a non-zero transition dipole matrix element, which is defined as

$$\langle \Psi_i | er | \Psi_j \rangle = \int_{-\infty}^{\infty}\int\int (\Psi_i \; er \; \Psi_j)\, dx\, dy\, dz \neq 0 \tag{3.7}$$

where e is the electron charge, r is its displacement from the atom's center of mass,

and Ψ_i and Ψ_j are the eigenfunctions of the initial and final states of a possible transition. If this matrix element is non-zero then the electron may make a transition between these two states by absorbing or emitting dipole radiation.

However, this simplified view of quantum mechanics does not address the cause of the splitting of spectral lines emitted in transitions to or from p and d-orbitals. This splitting is called fine structure and is observable using spectrometers of moderate resolution. This splitting is shown in the energy diagram for cesium in Figure 3.4. The energy levels are expressed in wavenumbers (σ) which are calculated from the expression

$$E = h\nu = \frac{hc}{\lambda} = hc\sigma \quad . \tag{3.8}$$

The energy levels are relative to the ground state. This splitting creates a multitude of transition wavelengths, as they are shown in Figure 3.5.

The splitting can be explained if it is assumed that the electron possesses spin angular momentum coupled to the orbital angular momentum, symbolized by the quantum numbers s and l respectively. Note: In this dissertation, quantum numbers will appear in italics (s) and the vector will appear in bold (s). The electron's total angular momentum is then the vector sum $\mathbf{j}=\mathbf{l}+\mathbf{s}$, and the new quantum number j is called the inner quantum number. The inner quantum number falls in the range of $|l+s| > |j| > |l-s|$. The convention with quantum numbers when dealing with the entire atom is

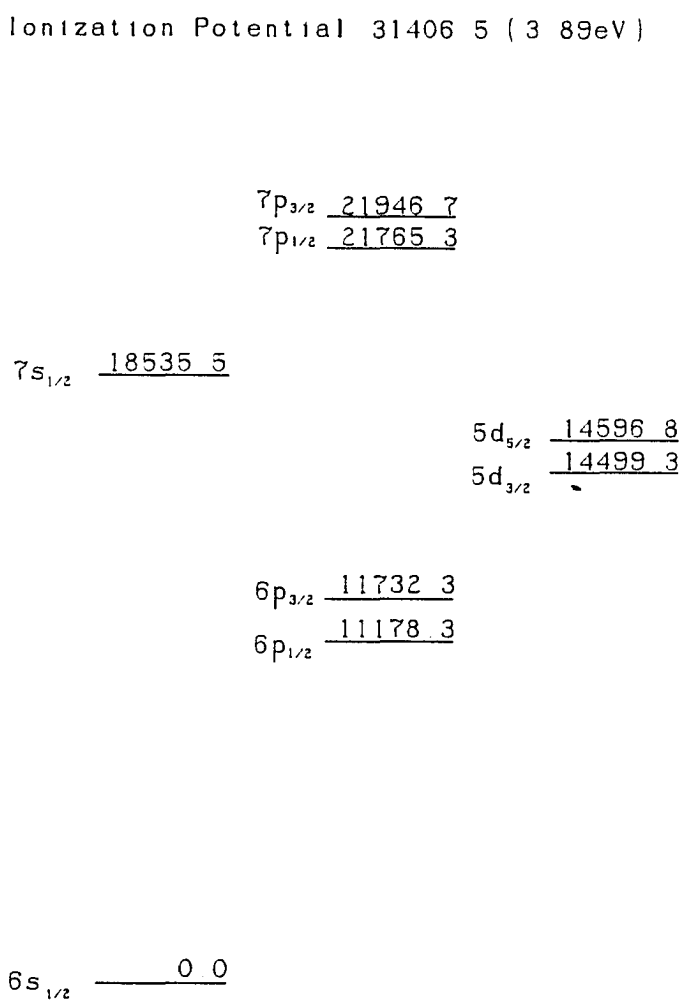

Figure 3.4. Cesium energy level diagram[20,21] in units of cm^{-1}.

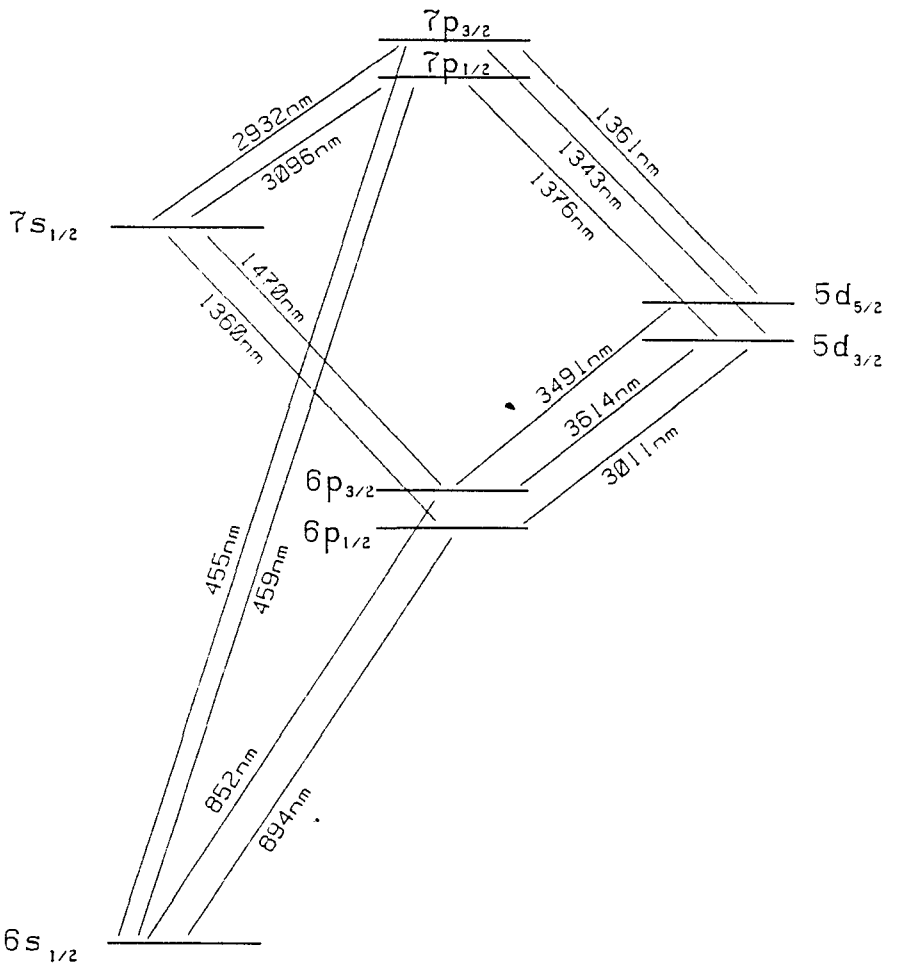

Figure 3.5. Transition wavelengths for the lower excited states of cesium[22].

to use the uppercase counterpart of the specific quantum number (ie. replace j with J).

For cesium, a solitary outer electron surrounds a core having the configuration of the noble gas Xenon. The core has no net spin so the total spin of the atom is due to this single outer electron; the atom thus has $S=½$. The ground state and all other s-orbitals are therefore singlets according to this model of ls-coupling. The p-orbitals have j values of $|l+s| = {}^3/_2$ and $|l-s| = {}^1/_2$, and the d-orbitals have j values of ${}^5/_2$ and ${}^3/_2$. The selection rules on the inner quantum number are

$$\Delta J = 0,\pm 1 \tag{3.9}$$

with the exception that transitions from $J=0$ to $J=0$ are not allowed. In general the splitting of the d-orbitals is small in comparison with that of the p-orbitals.

The isotope effect produces an even finer splitting of the spectral lines. Different isotopes have different centers of mass, different values for the reduced mass of the system, and therefore slightly different energies. Heavier isotopes will have the same characteristic spectrum except with a small shift toward lower frequencies. For hydrogen this shift is about 5 cm^{-1}, but for heavier elements this shift is significantly smaller. Cesium only has one stable isotope, Cs^{133}, so it does not show the such effects.

There is, however, splitting of the fine structure of cesium. The first

explanation of this phenomenon was offered by Pauli, who suggested that the nucleus possesses angular momentum, with quantum number I, which couples with the angular momentum of the electron. The total angular momentum for the whole atom is **F**, which is the vector sum of **I+J**. The quantum number F is bounded by the two quantities $|J+I|$ and $|J-I|$. The observed value of the nuclear spin for cesium[23] is $I={}^{7}/_{2}$. The splittings of the energy levels for the transitions leaving the ground state of cesium are calculated below. The selection rule for F is

$$\Delta F = 0,\pm 1 \tag{3.10}$$

with the exception that a transition from $F=0$ to $F=0$ is not allowed. Figure 3.6 shows the allowed transitions from the ground state to the 7p-orbitals. The relative intensities of the emission lines depend on the exact means of excitation. It is now necessary to indicate that the energy-level values given in Figure 3.4 are actually the centroid values, or weighted mean values that are averaged over the hyperfine structure.

The energy splitting between hyperfine levels is calculated as the departure from the centroid, or multiplet, level W_J. The energy[24,25] of a hyperfine structure level with quantum number F is

$$W_F = W_J + A\frac{C}{2} + B\,\frac{\frac{3}{4}C(C+1) - I(I+1)J(J+1)}{2I(I-1)J(J-1)} \tag{3.11}$$

where $C=F(F+1)-I(I+1)-J(J+1)$, and the constants A and B are the published hyperfine structure constants for cesium, as shown in Table 3.1. From these two

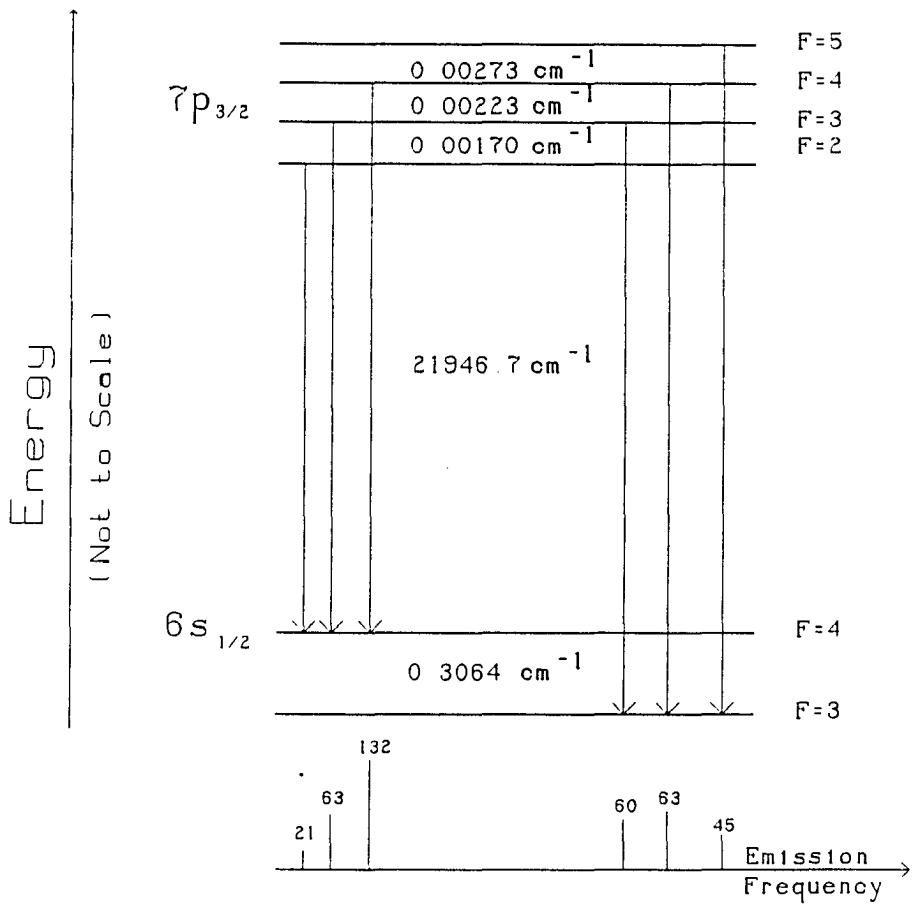

Figure 3.6. Allowed hyperfine transitions in the 455nm cesium line and their relative intensities.

constants the energy level splittings are calculated, as displayed in Table 3.2.

However, even with an understanding of hyperfine structure, a complete description of the spectrum has not yet been presented. The spectrum is completely described when line placement, lineshape and relative line intensities are known. The next few sections deal with the lineshape, or absorption (emission) distribution, that is centered about each of these line centers.

Hyperfine Structure Constants[26]		
multiplet level	A [MHz]	B [MHz]
$5d_{5/2}$	22.2	-
$6s_{1/2}$	2298.2	-
$6p_{1/2}$	291.90	-
$6p_{3/2}$	50.34	-0.38
$7s_{1/2}$	546.3	-
$7p_{1/2}$	94.35	-
$7p_{3/2}$	16.605	-0.15

Table 3.1. Hyperfine constants for Cesium

level pairs	separation [cm^{-1}]
$6s_{1/2}$ F=3,F=4	0.3064
$6p_{1/2}$ F=3,F=4	0.0388
$6p_{3/2}$ F=2,F=3	0.00513
F=3,F=4	0.00676
F=4,F=5	0.00830
$7p_{1/2}$ F=3,F=4	0.0126
$7p_{3/2}$ F=2,F=3	0.00170
F=3,F=4	0.00223
F=4,F=5	0.00273

Table 3.2. Calculated energy differences from hyperfine structure constants.

Section 4: Lorentz Broadening

We begin this chapter recognizing that the wavelengths previously tabulated for the energy level transitions of cesium represent the center wavelengths of distributions that have finite widths. In the next few pages, we show how two different phenomena, natural and collisional broadening, contribute to line broadening and then proceed through lineshape calculations. Natural broadening arises from the properties of spontaneous emission. The natural linewidth depends on the two states involved in the transition and typically represents the minimum possible linewidth. The second process, collision broadening, arises from Brownian motion. For both phenomena, each atom in an ensemble of atoms exhibits the same lineshape and line center. The response of the collection as a whole, being the sum of each atomic response, then shares the same lineshape. These phenomena produce homogeneous broadening and are responsible for the Lorentzian character of atomic spectra.

When modeling a physical phenomenon, it is typical to start with the simplest possible model and see how closely it mimics reality. The simplest realistic picture of an atom is known as the classical electron oscillator (CEO) model. The CEO model will provide a physical picture for the origin of the excitation frequency, the lifetime of an excited state, and the absorption lineshape of an atomic resonator.

The CEO model assumes that an atom is composed of a fixed nucleus that is surrounded by a mobile electron cloud. This electron cloud normally resides at an

equilibrium position symmetric with respect to the nucleus, but it may move from this position if acted on by an external force. An important external force is imposed on the electron cloud by the electric field of an incident electro-magnetic (EM) wave. The force that resists the movement of the electron cloud, the restoring force, is assumed to be linear with displacement. (This is analogous to an electron connected to the nucleus by a spring.) The equation of motion for an undriven oscillator is

$$m\frac{d^2x(t)}{dt^2} = -kx(t) \quad , \tag{4.1}$$

where the time dependent displacement is x, the electron mass is m, and the restoring constant is k. This differential equation has the following solution:

$$x(t) = x(t_0)(e^{i\omega_a t} + e^{-i\omega_a t}) \tag{4.2}$$

where the natural frequency of oscillation is

$$\omega_a = \sqrt{k/m} \quad . \tag{4.3}$$

The displacement of the positively charged nucleus and negatively charged electron cloud from their symmetrical equilibrium position creates an electric dipole whose amplitude is periodic, and the electric field that emanates from this dipole must then have the same frequency as the dipole displacement. It is this dipole emission that corresponds to the light wave generated in the atomic transition between two energy levels. The oscillation frequency, ω_a, and the energy emitted correspond to the transition frequency and the energy level difference between the upper and lower states,

respectively.

$$h\nu = E_{(upper\ state)} - E_{(lower\ state)} \tag{4.4}$$

Since the amplitude of oscillation is undiminished with time in this ideal case, the resonator emits an infinite amount of energy, a result inconsistent with experience. A damping term proportional to the electron velocity is included in the equation of motion to limit the total energy emitted by the oscillator, i.e.

$$\frac{d^2x(t)}{dt^2} = -\omega_a{}^2 x(t) - \gamma\frac{dx(t)}{dt} \quad . \tag{4.5}$$

The damping coefficient is γ, and the solution of this equation is

$$x(t) = x(t_0)\, e^{(-\frac{\gamma}{2} + i\omega_a')(t - t_0)} \quad , \tag{4.6}$$

where the exact resonance frequency is defined as

$$\omega_a' = \sqrt{\omega_a{}^2 - (\gamma/2)^2} \quad . \tag{4.7}$$

The total energy of the oscillator has two components,

$$U_{tot} = (Potential\ Energy) + (Kinetic\ Energy) \quad , \tag{4.8}$$

having an explicit temporal dependence of

$$U_{tot} = \frac{1}{2}m v(t)^2 + \frac{1}{2}kx(t)^2 = \frac{1}{2}m\left[\frac{d(x(t))}{dt}\right]^2 + \frac{1}{2}kx(t)^2 \quad . \tag{4.9}$$

Substitution of $x(t)$ and its first derivative into the above equation shows the energy

decay with time,

$$U_{out} = U(t_0)\, e^{-\gamma(t-t_0)} = U(t_0)\, e^{-(t-t_0)/\tau} \quad . \tag{4.10}$$

Here γ appears as an energy decay rate, thus defining τ as the energy decay time. The energy decay time of the oscillator is equivalent to the lifetime of the excited state. The radiated energy is called spontaneous emission, or fluorescence.

The primes were omitted in the above equations due to the frequency approximation,

$$\omega_a' = \omega_a \quad . \tag{4.11}$$

This is legitimate for most atomic transitions since they are quite underdamped, corresponding to a small value for γ.

Classical electromagnetic theory predicts a value of

$$\gamma_{CEO} = \frac{e^2 \omega_a^{\,2}}{6\pi\epsilon mc^3} \quad , \tag{4.12}$$

according to the CEO model based on the energy emitted by an oscillating electric dipole. However, a quantum mechanical treatment must be followed to account for the subtleties of dipole transitions. For example, there is no dipole emission unless the following transition rules are obeyed.

$$\Delta l = \pm 1 \quad , \qquad \Delta m = 0, \pm 1 \tag{4.13}$$

where l and m are the angular momemtum and spin quantum numbers as presented earlier. The value of γ that emerges is

$$\gamma_{ij} = \frac{8\pi^2}{\epsilon\hbar\lambda^3} \left| \int_{\tau} \Psi_i er \Psi_j^* d\tau \right|^2 \equiv A_{ij} \quad . \tag{4.14}$$

where Ψ_i and Ψ_j are the wavefunctions for the upper and lower energy states, respectively, and er, the product of electron charge and position, is the dipole operator. The last symbol, A_{ij}, is included to show how the Einstein A-coefficient is defined. This coefficient may be calculated if the wavefunctions are known, but it may be experimentally determined as it is the value for the decay rate for a purely radiative transition. The values of γ, or A_{ij}, can be considered the transition probabilities and have units of sec^{-1}. The transition probabilities for cesium are provided in Table 4.1.

A more detailed analysis of the transition between two energy states refines the value for the energy decay time. For spontaneous emission the total decay rate is dictated solely by the upper level.

$$\gamma_{tot} = A_i \tag{4.15}$$

where A_i denotes the sum of all radiative pathways from state i to lower states k.

$$A_i = \sum_k A_{ik} \quad , \quad A_j = \sum_k A_{jk} \tag{4.16}$$

If nonradiative transitions are included, such as de-excitation due to collisions with other gas species or the walls of the container, then the final refinement of the decay rate is

$$\gamma_{tot} = A_i + \gamma_{(nonradiative)} \quad . \tag{4.17}$$

Table 4.1. Transition wavelengths and probabilities[27,28,29,30]

Transition	wavelength (nm)	transition probability [sec^{-1}]
$7p_{3/2}$ - $7s_{1/2}$	2932	4.01
- $6s_{1/2}$	455	1.9
- $5d_{5/2}$	1361	1.05
- $5d_{3/2}$	1343	0.11
$7p_{1/2}$ - $7s_{1/2}$	3096	3.54
- $6s_{1/2}$	459	0.95
-$5d_{3/2}$	1376	1.35
$7s_{1/2}$ - $6p_{3/2}$	1470	12.0
- $6p_{1/2}$	1360	5.5
$6p_{3/2}$ - $6s_{1/2}$	852	33.0
$6p_{1/2}$ - $6s_{1/2}$	894	28.0
$5d_{5/2}$ - $6p_{3/2}$	3491	0.84
$5d_{3/2}$ - $6p_{3/2}$	3614	0.*
- $6p_{1/2}$	3011	1.0

This contribution from nonradiative decay may be significant and is required, for example, for the operation of He-Ne lasers. This laser is excited by collisional transfer of energy with excited helium atoms. It depopulates the metastable lower state by collisional de-excitation with the walls. The nonradiative transitions for the cesium resonance, however, are insignificant. First of all, collisional transfer of energy to the residual gases is not possible since the energy released by a cesium atom does not match any of the possible residual gas transitions. Secondly, the likelihood of collisional transfer with the chamber walls is small.

Drawing now on data that is presented in a later chapter, at 100°C the average atom is moving at a rate of 250m/s and has an excited state lifetime of about 10ns. When a path of 2.5μm has been traversed by atoms having this lifetime, 1/e of the atoms will have decayed. Since the chamber is several orders of magnitude larger than this distance, the likelihood of an excited atom encountering a wall is negligible.

Up until now the atomic oscillator was assumed to be initially excited and not under the continual influence of an external field. This assumption is now relaxed, and a driving force is added to find the atomic frequency response to incident radiation and to calculate the absorption spectrum,

$$\frac{d^2x(t)}{dt^2} + \gamma_{CEO}\frac{dx(t)}{dt} + \omega_a{}^2x(t) = -\frac{e}{m}\mathrm{E}(t) \quad . \tag{4.18}$$

The macroscopic polarization of a collection of such atoms is

$$P = Nex \quad , \tag{4.19}$$

where N is the atomic number density. A harmonic form is assumed for the polarization,

$$P = \frac{1}{2}(\tilde{P}e^{i\omega_a t} + \tilde{P}^* e^{-i\omega_a t}) \quad , \tag{4.20}$$

where the tilde ($\sim$) indicates complex polarization. Using these two definitions, we can say

$$x = \frac{P}{Ne} = \frac{1}{2Ne}\left(\tilde{P}e^{i\omega_a t} + \tilde{P}^* e^{-i\omega_a t} \right) \quad . \tag{4.21}$$

Substituting this in (18), the driven oscillator equation, produces

$$(-\omega^2 + i\omega\gamma_{CEO} + \omega_a{}^2)\tilde{P} = \frac{Ne^2}{m}\tilde{\mathrm{E}} \quad . \tag{4.22}$$

The atomic susceptibility, χ, being proportional to the ratio of P/E, is also complex.

$$\tilde{\chi} = \frac{\tilde{P}}{e\tilde{\mathrm{E}}} = \frac{Ne^2}{me}\,\frac{1}{\omega_a{}^2 - \omega^2 + i\omega\gamma_{CEO}} = \chi' + i\chi'' \quad . \tag{4.23}$$

Here the near-resonance approximation is useful.

$$\omega_a^2 - \omega^2 = (\omega_a + \omega)(\omega_a - \omega) \approx 2\omega(\omega_a - \omega) \qquad (4.24)$$

This approximation is usually invoked since the atomic lines are very narrow. Real transitions have a very sharp resonance peak as quantified by the resonator quality factor, Q, defined as

$$Q = \frac{\omega_a}{2\gamma} \quad . \qquad (4.25)$$

The atomic susceptibility is then only non-zero in the neighborhood of the resonance frequency.

The imaginary part of the susceptibility, χ'', leads to absorptance and has the form

$$\chi'' = \frac{Ne^2}{m\epsilon} \frac{\omega\gamma_{CEO}}{(\omega_a^2 - \omega^2)^2 + \omega^2\gamma_{CEO}^2} \quad . \qquad (4.26)$$

The absorption coefficient, in units of $length^{-1}$, is

$$\alpha(\omega) = \frac{\omega}{c}\chi'' = \frac{Ne^2}{\epsilon mc} \frac{\gamma_{CEO}}{[2(\omega - \omega_a)]^2 + \gamma_{CEO}^2} \quad . \qquad (4.27)$$

By defining

$$x = \frac{2(\omega - \omega_a)}{\gamma} \quad , \tag{4.28}$$

the Lorentzian behavior of the absorption becomes evident.

$$\alpha(x) = \frac{Ne^2\pi}{\epsilon mc\gamma_{CEO}}\left(\frac{1}{\pi}\frac{1}{1+x^2}\right) \tag{4.29}$$

A term commonly used to quantify the relative absorption strength for a transition is the integrated absorption, α_{tot}, which is defined as the integral,

$$\alpha_{tot} = \int_{-\infty}^{\infty} \alpha(\nu)\, d\nu \quad . \tag{4.30}$$

This is evaluated after converting the extinction coefficient to linear frequency, ν,

$$\nu = \frac{\omega}{2\pi} \quad , \tag{4.31}$$

and integrating, giving a value of

$$\alpha_{tot} = \frac{Ne^2}{\epsilon mc} \quad . \tag{4.32}$$

This last section has ignored the quantum mechanical distinction that was previously made between γ and γ_{CEO}. The integrated absorption is corrected for this using the substitution

$$\frac{e^2}{m} \rightarrow \frac{e^2\mathcal{F}}{m} \quad , \tag{4.33}$$

where the oscillator strength, $\mathcal{F}$, is defined below as

$$\mathcal{F} = \frac{\gamma_{tot}}{3\gamma_{CEO}} \quad . \tag{4.34}$$

Substituting the definition of γ_{CEO}, equation (4.12), gives the integrated absorption in final form.

$$\alpha_{tot} = \frac{Nc^2\gamma_{tot}}{2\pi\nu^2} \quad . \tag{4.35}$$

Collision Broadening

The second type of homogeneous broadening is collision broadening. The remainder of this section is devoted to discussing its origin and calculating its linewidth.

The previous calculation of the susceptibility was performed by computing the polarization for N dipoles per unit volume in phase with one another. There was no discussion of a possible distribution of phases for the collection of dipole radiators, which is reasonable because oscillators out-of-phase with an external driving force with frequency ω_d will asymptotically approach an oscillation state that has the a frequency of ω_d and a specific phase relation to it, φ_d. This is shown starting with the equation

of motion for a damped, driven harmonic oscillator,

$$m\frac{d^2x(t)}{dt^2} + \gamma\frac{dx(t)}{dt} + kx(t) = F_o e^{i(\omega_d t + \theta)} \quad , \tag{4.36}$$

where θ is the phase of the driving force at t=0. The transient solution eventually decays to zero leaving only a steady-state displacement of the following form,

$$x(t) = x_{max} e^{i(\omega t + \theta')} \quad , \tag{4.37}$$

where θ' is the phase and x_{max} is the amplitude of the dipole displacement. Substitution of this into the above equation and separating out the real and imaginary parts yields

$$x_{max}(k - m\omega^2) = F_o \cos(\varphi_d) \tag{4.38}$$

$$\gamma\omega x_{max} = F_o \sin(\varphi) \quad , \tag{4.39}$$

where φ_d is the relative phase lag between the driving force and the oscillator displacement, such that $\varphi_d=\theta-\theta'$. From these parametric expressions one obtains

$$\tan(\varphi_d) = \frac{\gamma\omega}{k - m\omega^2} \quad . \tag{4.40}$$

So, regardless of initial oscillator phase or displacement, all oscillators approach a steady state solution where they are in phase, or "aligned". Therefore the steady state polarization could be written as

$$P(t) = Nex(t) \quad , \tag{4.41}$$

where N is the total cesium atom density.

Collision broadening has its origin in the dephasing action of random collisions that occur in gases due to Brownian motion. This effectively changes the number of dipoles that are in phase with each other. This phase disturbance is caused by the nature of the collision itself. As two atoms approach each other, the actual energy levels, hence resonance frequencies, are perturbed due to the interaction of the electron clouds and nearby nuclei. The radiating oscillator continues to emit during this process but at a slightly different frequency than before. After the collision event the dipole emits at its original frequency, but now with a changed phase with respect to the phase of an uncollided dipole.

There are several models that approximate the collision process. In the simplest model, the collisions have zero duration, after which atomic emission advances by a large relative phase ($\Delta\theta >> 2\pi$). The net averaged polarization contribution of atoms that suffer a collision is then,

$$P_{collided}(t) = N_{collided}(t)\ e\ \langle x(t)\rangle_{all\ phase} \quad , \tag{4.42}$$

The displacement is periodic and has a random phase shift $\Delta\theta$, therefore

$$P_{collided}(t) = N_{collided}(t)\ e\ \langle x\cos(\omega t + \Delta\theta)\rangle_{allphase} \quad , \tag{4.43}$$

$$P_{collided}(t) = N_{collided}(t)\ e\ x\ \langle \cos(\omega t + \Delta\theta)\rangle_{allphase} = 0 \quad . \tag{4.44}$$

So, only the uncollided atoms contribute to the polarization,

$$P_{uncollided}(t) = N_{uncollided}(t)\ e\ x(t) \quad . \tag{4.45}$$

The uncollided atomic number density changes exponentially with time, and is dependent on the average collision time, denoted by convention as T_2, as shown,

$$\frac{dN_{uncollided}(t)}{dt} = -\frac{N_{uncollided}(t)}{T_2} \tag{4.46}$$

$$N_{uncollided}(t) = N_o\ e^{-\frac{t-t_o}{T_2}} \tag{4.47}$$

This result helps us find the net polarization which includes collision broadening. Substituting this into equation (4.45) gives

$$P(t) = P_o\ e^{-(\gamma/2 + 1/T_2)(t - t_o) + i\omega_a(t - t_o)} \quad . \tag{4.48}$$

This decays with a rate of $\gamma/2 + 1/T_2$, more rapidly than the single dipole decay rate of $\gamma/2$. Comparison with equation (4.36), which describes the driven harmonic oscillator, indicates that this polarization is the solution to the following differential equation.

$$\frac{d^2P(t)}{d^2t} + (\gamma + \frac{2}{T_2})\frac{dP(t)}{dt} + \omega_a{}^2P(t) = \frac{Ne^2}{m}E(t) \tag{4.49}$$

From this we find the resulting absorption lineshape is again Lorentzian.

$$\alpha(\omega) = \frac{Ne^2}{\epsilon mc} \frac{\gamma + \frac{2}{T_2}}{[2(\omega - \omega_a)]^2 + (\gamma + \frac{2}{T_2})^2} \quad . \qquad (4.50)$$

It is necessary to mention alternative assumptions and their effects. First, we assumed the atoms did not become realigned, or poled, after collision. The phasing (alignment) and dephasing phenomena are competing processes. At typical pressures of a fraction of an atmosphere, the dephasing events occur with such frequency that repoling usually occurs only in very high intensity fields. Since the region of interest involves low field intensities and high collision rates, poling will not occur. Secondly, the choice of collision duration and phase change alters the results slightly. For a Lorentzian lineshape to appear, the collisions must be effectively of zero duration. In this case the phase change may be either completely randomizing[31] ($\Delta\theta >> 2\pi$) or slightly randomizing[32,33] ($\Delta\theta < 2\pi$). If the collision has finite duration, the lineshape appears to exhibit dispersion, skewing it slightly[34,35,36,37], and a spectral shift. The distribution to either side the central wavelength appears to have a width proportional to the frequency offset, as observed by Walkup et al. (1980) and reproduced in Figure 4.1. The relative deviation from the Lorentzian is graphed in Figure 4.2. As a function of detuning, Δ, which is defined as $\Delta = \nu - \nu_o$, the distribution appears to have a width of

$$\gamma(\Delta) = \gamma_{natural} + \gamma_{collisional}*(1-b\Delta) \quad , \tag{4.51}$$

where $\gamma_{collisional}$ is the collision broadened width and b is the asymmetry parameter. This is not included in the analysis done for this dissertation because it is a small effect. It can only be easily seen in the wings of the Lorentzian line, which in our case is not significant since the medium is predominantly Doppler broadened, a phenomenon discussed later. The shift of the spectral line is due to the difference in the energy level curves of the upper and lower states as a function of the interatomic separation between a Cs atom and its collision partner. The direction of the shift may be to either higher or lower wavelengths depending on the collision partner. The shift coefficients are listed in Table 4.2.

All that remains is to find the value of T_2, or γ. A rough estimate of the collision time may be made if one makes the "billiard-ball", or hard sphere, approximation combined with basic knowledge of gas kinetics. The "billiard-ball" approximation indicates the mean free path length between collisions. The particle velocity, derived using basic laws from gas kinetics, determines the mean free time between collisions, T_2.

In the "billiard-ball" approximation, one assumes that two atoms collide if they have a separation, l, less than the sum of their atomic radii,

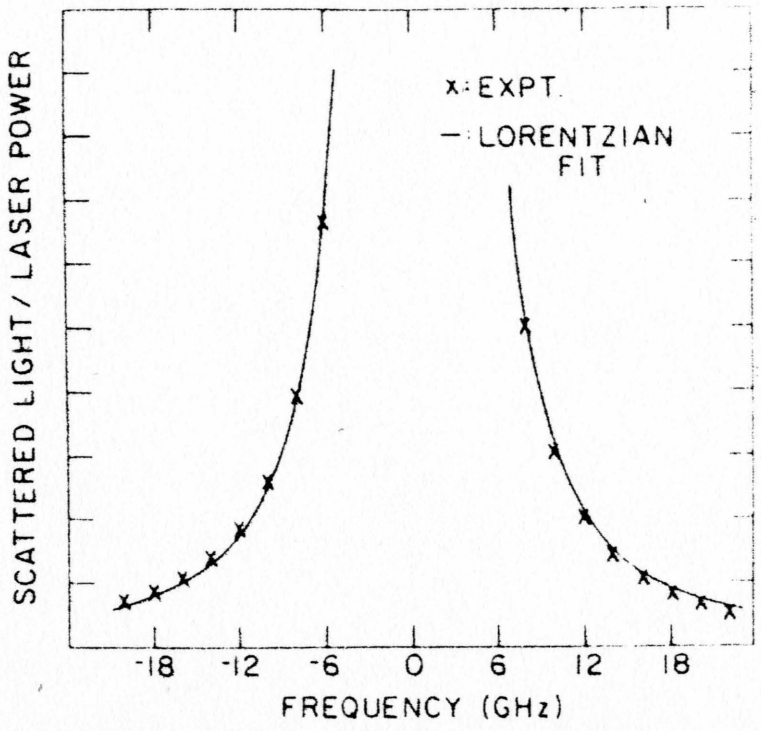

Figure 4.1. Skewed Lorentzian lineshape due to collisional broadening.

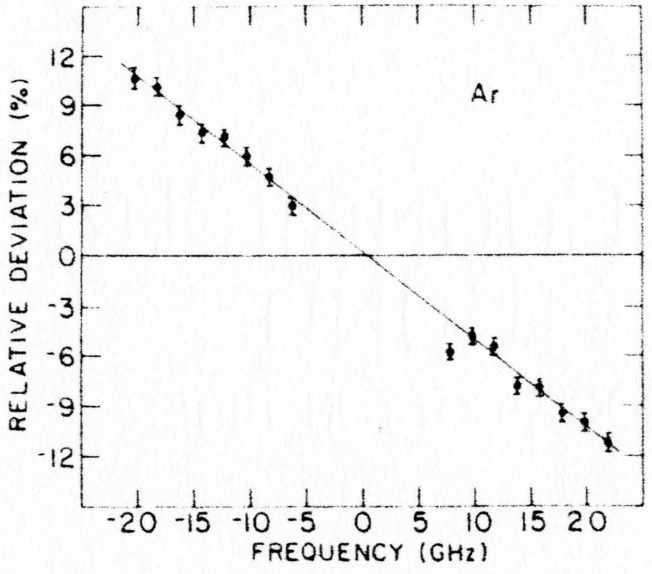

Figure 4.2. Relative deviation of experimental absorption line from best-fit Lorentzian lineshape.

Table 4.2. Shift coefficients (σ/n) for cesium[38] units of [10^{-20} cm^{-1} /cm^{-3}]				
	455nm	459nm	852nm	894nm
Helium	0.73	1.50	0.39	0.67
Neon	-0.56	0.00	-0.43	-0.29
Argon	-1.55	-1.63	-0.75	-0.89
Krypton	-	-	-0.81	-0.27
Xenon	-1.67	-1.66	-0.91	-0.84

$$l < r_{Cs} + r_{c.p.} \quad . \tag{4.52}$$

Cs is always in this equation since we are calculating the mean free path (MFP) of a cesium atom in the gas. The second term, $r_{c.p.}$, represents the radius of one of the many collision partners that exist in the gas, including other Cs atoms. The cross sectional area for this combination of atoms is

$$\sigma_{collision} = \pi(r_{Cs} + r_{c.p.})^2 \quad . \tag{4.53}$$

The density of the collision partners and $\sigma_{collision}$ determine the MFP. Consider a slab of gas having thickness dx and collision partner density $N_{c.p.}$. If the frontal area of the slab is unity, the probability of impacting an atom within the slab is

$$N_{c.p.}\sigma_{collision}dx \quad . \tag{4.54}$$

The MFP in such a medium is then

$$MFP = \frac{1}{\sigma_{collision} N_{c.p.}} \quad . \tag{4.55}$$

To obtain the mean free time (MFT) between collisions one only needs to know the relative velocity between the collision partners and the MFP. From Maxwell-Boltzmann gas kinetics the rms velocity, v_{rms}, between two similar atoms is

$$V_{rms} = \sqrt{\frac{8k_BT}{\pi m}} \quad . \tag{4.56}$$

The general case involving dissimilar atoms uses the reduced mass of the two species, μ,

$$V_{rms} = \sqrt{\frac{8k_BT}{\pi}\left(\frac{1}{m_{Cs}} + \frac{1}{m_{c.p.}}\right)^{1/2}} = \sqrt{\frac{8k_BT}{\pi\mu}} \quad . \tag{4.57}$$

The desired MFT, or T_2, is then

$$T_2 = \frac{MFP}{V_{rms}} = \frac{\sqrt{\mu}}{\sqrt{8\pi k_BT}\, N_{c.p.}(r_{Cs} + r_{c.p.})^2} \quad . \tag{4.58}$$

This procedure only gives approximate values for T_2, however, mostly due to the "billiard-ball" approximation. The MFT for atoms changes greatly under varied circumstances and for a resonant collision, a collision in which energy is transferred between collision partners, may be several orders of magnitude smaller than this estimate.

Instead of deriving the collision time from first principles and vaguely related constants one typically finds γ from experimental data. Data is usually published in the form of constants to the Stern-Vollmer equation for pressure broadening,[39]

$$\gamma = A + \sum_i B_i P_i \quad . \tag{4.59}$$

The constant term, A, is the natural width and the second term of the equation is the sum of contributions from all gases present, using their respective broadening coefficients, B_i, and pressures, P_i. The coefficients for cesium are in Table 4.3 for various noble gas collision partners. The broadening caused by noble gases is primarily due to van der Waals interactions, and therefore are dependent on the polarizability of the collision partner. The heavier noble gases, having a larger polarizability, have larger pressure-broadening coefficients than their lighter counterparts.

The region of interest for this dissertation lies in the temperature range 20°C to 120°C, and in the cell buffer gas pressure range 0 and 100 torr, as measured at room temperature (22°C). Figure 4.3 is a contour plot that shows the magnitudes of collisional broadening that are generated over these ranges using a neon buffer gas. Figure 4.4 shows the absorption FWHM for a Cs cell having a neon fill pressure of 30 torr with better resolution.

Table 4.3. Broadening coefficients for cesium[40]
Half Width at Half Maximum [10^{-20} cm^{-1} / cm^{-3}]
(value valid at temperature[°K] in parentheses)

	455nm	459nm	852nm	894nm
Helium	3.45 (400)	4.40 (400)	1.36 (295)	0.98 (295)
Neon	1.62 (380)	1.75 (395)	0.53 (295)	0.51 (295)
Argon	-	3.18 (400)	1.16 (295)	1.0 (295)
Krypton	-	-	0.55 (295)	1.01 (295)
Xenon	2.60 (380)	3.0 (380)	2.93 (295)	1.09 (295)

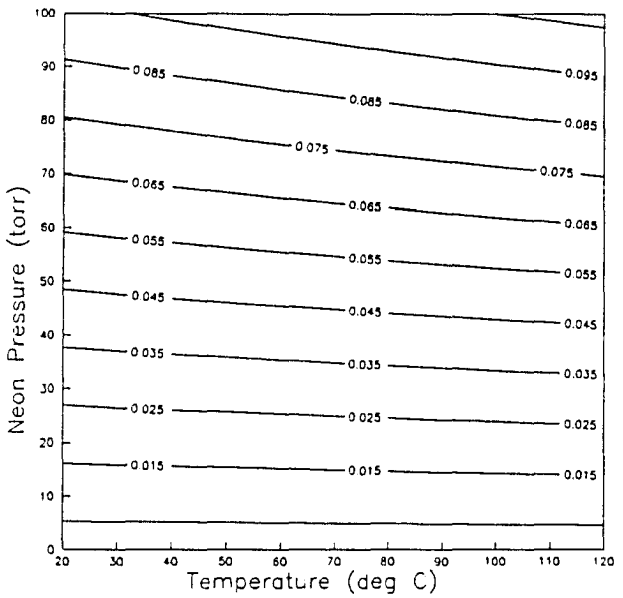

Figure 4.3. Contour plot of the collision broadened FWHM [cm^{-1}] for the 455nm cesium line. The neon pressure is the pressure as measured at room temperature (22°C).

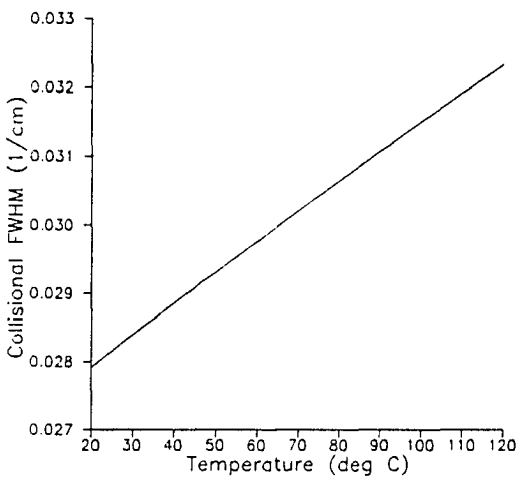

Figure 4.4. Collision broadened FWHM vs. temperature of the 455nm cesium line using 30 torr neon buffer gas.

Section 5: Doppler Broadening

In contrast to homogeneous line broadening, in which every atomic oscillator has an identical response, inhomogeneous broadening arises when the ensemble is composed of individual oscillators having varied responses. The following section will discuss this phenomenon, starting with the offset of an individual oscillator and proceeding with a calculation of the contribution of inhomogeneous broadening to overall absorption lineshape of a large collection of oscillators.

Even in a medium with a uniform composition, every atom does not have the same resonance response due to a number of factors. First, the energy levels of an atom depend on its immediate surroundings. In solids, the local interactions due to strain, impurities and dislocations cause identical atoms to have different resonance frequencies. Inhomogeneous broadening also occurs if the atoms in the medium are moving randomly. For example, when light is incident on such a medium, each atom experiences radiation in its own inertial reference frame which is frequency shifted an amount depending on its relative velocity. In solids this is associated with phonon propagation and in gases with Brownian motion.

The resonance frequency shift of a particular atom moving in the x-direction, away from the radiation source, at a velocity v_x follows the Doppler formula

$$\nu = \nu_o \sqrt{\frac{1-v_x/c}{1+v_x/c}} \quad . \tag{5.1}$$

This formula is calculated from the Lorentz coordinate transformation relating the speed of light, c, the source velocity, v_x, and the source and shifted frequencies ν_o and ν, respectively.

The total response of the medium as a whole is found as the sum of the individual atomic responses and is therefore dependent on the probability distribution of the velocities. For atoms in a dilute gas at thermal equilibrium, velocities follow the Maxwell-Boltzmann (M-B) distribution

$$p_V(v)d^3v = \left(\frac{m_{Cs}}{2\pi k_B T}\right)^{\frac{3}{2}} e^{-\frac{m_{Cs}v^2}{2k_B T}} d^3v \quad . \tag{5.2}$$

where cesium's atomic mass is m_{Cs}, the absolute temperature is T and the Boltzmann constant is k_B.

The above M-B distribution is not useful, as it stands, for finding the Doppler shift because the Doppler formula uses only the projected velocity v_x. Only the velocity component along the line connecting the atom and the photon source contributes to the Doppler shift. The M-B distribution must be integrated over the velocities perpendicular to v_x to find the one dimensional distribution denoted by $p_{vx}(v_x)$.

$$p_{V_x}(v_x)\,dv_x = \int_{v_z}\int_{v_y} p_V(v)d^3v = \left(\frac{m_{Cs}}{2\pi k_B T}\right)^{1/2} e^{-\frac{m_{Cs}v_x^2}{2k_B T}}\,dv_x \quad . \tag{5.3}$$

The necessary tools to perform the calculation of the lineshape are now assembled but one approximation makes this process more tractable. For small velocities ($v << c$) equation (5.1) simplifies to

$$\nu = f(v_x) = \nu_0(1 - v_x/c) \quad . \tag{5.4}$$

With the average kinetic energy of a particle in a gas being independent of its composition,

$$\overline{\frac{1}{2}m_{Cs}v_x^2} = \frac{1}{2}k_B T \quad . \tag{5.5}$$

We find that a Cs atom in a 100 °C vapor has an average kinetic energy of 0.03 eV, and therefore has an average velocity of 250 m/sec (roughly equal to $10^{-6}c$), well within the constraint on velocity.

The transformation from a probability law for one dimensional velocity to the frequency shift using this approximation as follows, using the procedure outlined in appendix A.

$$p_\nu(\nu)d\nu = p_{V_x}(v_x)dv_x \tag{5.6}$$

$$p_\nu(\nu) = \frac{p_{V_x}(f^{-1}(\nu))}{\left|\frac{d\nu}{dv_x}\right|} \tag{5.7}$$

where the inverse function is defined as

$$v_x = f^{-1}(v_x) = c(1-\nu_0/\nu) \quad . \tag{5.8}$$

The probability law for frequency is then

$$p_\nu(\nu)d\nu = \frac{c}{\nu_o}\left(\frac{m_{Cs}}{2\pi k_B T}\right)^{\frac{1}{2}} e^{-\frac{c^2 m_{Cs}}{2k_B T \nu_o^2}(\nu-\nu_o)^2} \quad . \tag{5.9}$$

This is a Gaussian function, and to be consistent with the definitions in Appendix A, the standard deviation σ_D has the value

$$\sigma_D = \frac{\nu_o}{c}\sqrt{\frac{k_B T}{m_{Cs}}} \quad . \tag{5.10}$$

Using this definition the Doppler lineshape takes the form used in Appendix A.

$$p_\nu(\nu)d\nu = \frac{1}{\sqrt{2\pi\sigma_D^2}} e^{-\frac{(\nu-\nu_o)^2}{2\sigma_D^2}} \quad . \tag{5.11}$$

The FWHM is therefore

$$FWHM = 2\frac{\nu_o}{c}\left(\frac{2k_bT}{m_{Cs}}\ln(2)\right)^{1/2} \quad . \tag{5.12}$$

The Doppler FWHM as a function of temperature is graphed in Figure 5.1 for the 455, 459, 852 and 894nm lines. The absorption at line center of a transition that only has Doppler broadening is

$$\alpha(\nu_o) = \frac{c}{2\nu_0}\sqrt{\frac{2m_{Cs}}{\pi k_B T}} * \textit{integrated absorption} \quad .$$

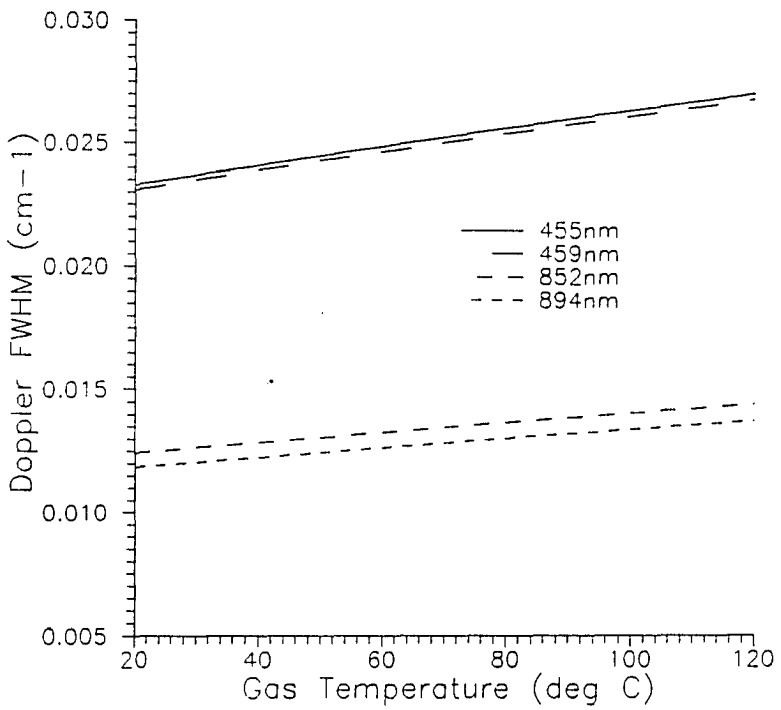

Figure 5.1. The Doppler FWHM for four emission lines of cesium.

Section 6: The Voigt Profile

Pure Lorentzian or pure Doppler broadened materials have absorption profiles with simple functional forms. However, profiles, in practice, almost always have finite contributions from both processes. Fortunately, the two processes are independent of one another. The atom emits, in its inertial reference frame, a Lorentzian distribution according to the homogeneous linewidth. The atom does this independently of its velocity relative to the laboratory frame of reference. Therefore the frequency shift from line center is just the sum of shifts from both contributions.

$$\Delta\nu_{total} = \Delta\nu_{Lorentz} + \Delta\nu_{Doppler} \quad . \tag{6.1}$$

The line function of the resulting distribution, called a Voigt profile, is then the convolution of the probability distributions of the two contributions.

$$p_V(\nu) = p_D(\nu) * p_L(\nu) \tag{6.2}$$

The Voigt profile has no simpler form, always being defined as an integral which must be solved numerically.

The Voigt profile may be conceived in two different ways. The first way was shown above, by thinking of the two processes as being independent and performing a convolution, written out explicitly as

$$p_V(\nu) = \int_{-\infty}^{\infty} p_D(\nu') \, p_L(\nu-\nu')d\nu' \quad . \tag{6.3}$$

Substitution of the Doppler and Lorentzian distributions gives

$$p_V(\nu) = \int_{-\infty}^{\infty} \frac{1}{\sqrt{2\pi\sigma_D^2}} e^{-\frac{\nu'^2}{2\sigma_d^2}} \frac{a}{\pi} \frac{1}{a^2+(\nu'-\nu)^2} \, d\nu' \quad . \tag{6.4}$$

An equally valid approach is to view this problem using conditional probabilities[41,42]. We first define the conditional probability $p(A|B)$ as the probability of the occurence of A given the occurence of B. If the atom's projected velocity is v_x, then the Lorentzian distribution, with a Doppler shifted offset, is shown below.

$$p_L(\nu|v_x) = \frac{a}{\pi} \frac{1}{a^2+\left(\nu - \nu_o\left[1-\frac{v_x}{c}\right]\right)^2} \tag{6.5}$$

where the offset appears as the frequency term $v_x\nu/c$. The Voigt distribution is then found using the partition law,

$$p_V(\nu) = \int_{-\infty}^{\infty} p_L(\nu|v_x)p_D(v_x)dv_x \quad , \tag{6.6}$$

which yields the same integral as above.

The Voigt profile may be approximated under certain conditions. The first two

are inherent to the convolution process. If a wide function is convolved with a very narrow function, then the result is that the wide function is essentially reconstructed. So if the Lorentzian distribution is narrow relative to the Doppler, then the convolution yields a function very much like the original Doppler distribution; this is the Doppler limit. Similarly, in the collisional limit, the Doppler width is relatively small compared to the Lorentzian width and the resultant distribution is nearly Lorentzian.

The last approximation that may be invoked is that if one is concerned with the profile out in the far wings, i.e. for frequency offsets much greater than either line width. The lineshape there is nearly Lorentzian, regardless of which component is narrower. Here, the product of the two separate functions only is significant near the center of the Gaussian function, due to the rapid fall-off of the Gaussian function relative to the broad wings of the Lorentzian.

Section 7: Simulation of Atomic Absorption and Gas Kinetics

The simulation of atomic absorption/emission in a gas is greatly simplified by the independence of the processes involved. It is their independence that makes it possible to discuss the simulation as a string of successive events. The discussion and derivation of the equations used in the actual computer code is reserved for Appendix A so that the processes themselves may be reviewed and interpreted in this section.

A rough outline of the sequence of events describing the interaction of a photon and an enveloping gas begins by considering the photon's position, direction and frequency. The photon travels a distance characteristic of the absorption of the gas before it is absorbed, exciting a Cs atom from the ground state. If the atom ends up in a highly excited state, then its relaxation pathway may lead to various intermediate energy levels or may lead directly to the ground state. The excited atom remains in its elevated energy state for a short time before transitioning to a lower state, leading to an effect known as pulse broadening. When the atom finaly emits a photon, the steps just described are repeated until specific boundary conditions are satisfied. For example, the photon may escape from the gas or be absorbed at a partially reflecting interface. The following is an in-depth look at all of the processes involved, the assumptions made, and their justifications where necessary.

Initial conditions

The photon initially has a well defined frequency as an output from a laser whose linewidth is negligible with respect to the absorption linewidth of the gas. The position and direction depend on the optical setup, and for the case of a narrow, collimated laser beam, both are well defined.

Absorption Distance

The probability law governing the distance that a photon will travel in a medium having an absorption α, follows Beer's law,

$$p_X(x) = \alpha e^{-\alpha x} \quad , \tag{7.1}$$

where α is determined from the amplitude of the Voigt profile at the photon frequency.

Photon Path

Upon entering the gas (or being re-emitted) the photon travels a straight, undeviated path to the location where it is absorbed by another atom except for directional changes that occur upon reflection by the walls of the container that holds the gas.

Photon "Intensity"

The photons in this simulation are absorbed and re-emitted by the gas without loss. That is to say that the atomic transition process is without absorptive loss mechanisms. The energy absorbed by the atom is returned in the form of one or more

photons. However, there are losses associated with any reflection from a surface. There are two ways to incorporate losses in a simulation. The first is an "all or nothing" approach which more closely resembles what really occurs when light hits a partially absorbing reflector. A single photon is either fully reflected, transmitted or absorbed at an interface. One calculates the probability of reflection and either "reflects" or "absorbs" the photon depending on the outcome of a random draw. If absorbed, the simulation returns to the initial input conditions and continues with another photon. However, this method is computationally inefficient, requiring the program to go through many steps without promise of any output. The second method treats the incident photon as a group of photons. The "intensity" of this photon group represents the number of photons remaining. The group experiences a loss in numbers when it encounters absorption but is never completely extinguished, so that some output is recorded for every run computed.

Information Contained in Atomic Absorption

The frequency of the incident photon actually provides information on the velocity of the absorbing atom. This is shown here for two cases. The first involves a limiting case where the Voigt profile is essentially Gaussian. The second is the general case where both Gaussian and Lorentzian broadening are present.

Consider the case where the Lorentzian width is infinitely narrow and Doppler broadening is present. In the inertial reference frame of the atom the absorption

response is a delta-function centered at the transition frequency. An atom will absorb radiation only if it has the correct velocity in the direction of the incident photon, v_x, to Doppler shift the incident photon to its exact transition frequency. This constrains the velocity in one direction only. The velocity components in the other two dimensions are unknown and are assumed to be characteristic of Maxwell-Boltzmann (M-B) statistics.

If the Lorentzian width is considered to be finite the above concept is still valid and a representative value of v_x is obtainable; however, one needs to interpret the outcome of the convolution process. As described before, the absorption lineshape is a convolution of the Gaussian and Lorentzian functions. A review of the convolution shows it to be of the form

$$p_{Voigt}(\nu) = \int_{-\infty}^{\infty} p_{Gaussian}(\nu') \, p_{Lorentzian}(\nu - \nu') \, d\nu' \quad . \tag{7.2}$$

This is the integrated product of two functions, the second of which is inverted and shifted by an amount ν. The two functions are shown graphically in Figures 7.1 (a) and (b) where the Lorentzian is the inverted and shifted function. Figure 7.1 (c) is the product of these two functions and its area corresponds to the value of $p_{Voigt}(\nu)$.

Interpreting this product as an un-normalized probability distribution in ν' gives information about v_x. Being a probability distribution, values of ν' are simulated using

occurs at the point $\nu' = a$ will become obvious shortly.

From here on, the lineshape will be discussed in terms of offset, or detuning from line center. As in the discussion of the Voigt profile, one realizes that an emission frequency offset of ν is obtained if the Lorentzian contribution to the offset is $\nu - a$ and the Gaussian contribution is a. This occurs since the total offset is the sum of the two contributions. Of course this result holds for any chosen value of a. Figures 7.1 (a), (b), and (c) graphically show the two contributions to the offset, since the distance in frequency from the point $\nu' = a$ to line center is a for the Gaussian plus $\nu - a$ for the Lorentzian. Once a value of a has been determined, as through a simulation, the contribution due to the Doppler shift is known and v_x is known through application of the Doppler formula.

Atomic Emission

The emission process is assumed to radiate uniformly into 4π steradians. The emission frequency in the reference frame of the atom follows the Lorentzian distribution according to the specific emission parameters, such as wavelength and Einstein A-coefficient. Once the emission direction and velocity vector of the emitting atom have been determined, the emission frequency in the lab reference frame is known.

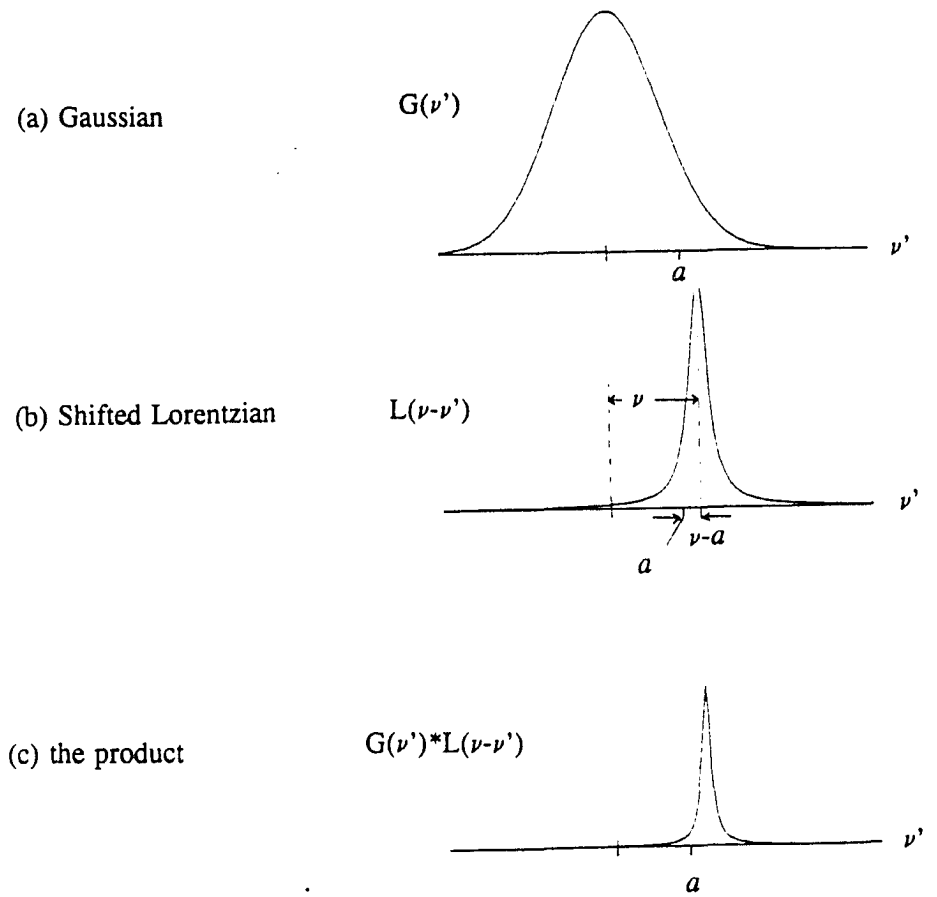

Figure 7.1. Interpretation of a convolution for determining a probability distribution on the velocity of an atom given the frequency offset from line center of the incident photon. The product, (c), is this probability distribution.

Recoil Effects

The atom experiences changes in velocity when it emits or absorbs a photon and when it collides with another atom. The recoil effects due to emission are significant under certain circumstances. Laser cooling, a technique for capturing and isolating single atoms[43,44], is based on this effect. The momentum transferred by emitting a photon is

$$momentum\ change = h/\lambda \tag{7.3}$$

where h is Planck's constant. For a Cs atom initally at rest the velocity change upon emission (absorption) of a 455nm photon is

$$velocity = \frac{h}{m_{Cs}\lambda} = 6.5*10^{-3}\ m/s \tag{7.4}$$

Since this change in velocity is very small in comparison to the width of the thermal velocity distribution, it is omitted from all further calculations.

The change in velocity due to collisions with other atoms is quite significant and may not be discounted. Collisions by their very nature tend to randomize the velocity vector of an atom. It is clear that multiple collisions will remove any correlation between initial and final velocity; it is therefore easy to simulate this since Gaussian random values may be assigned to all velocity components. The change in velocity after only one collision is much more difficult to describe. Since the likelihood of

hitting another atom is velocity dependent, the final velocity distribution is dependent on the initial velocity. An in-depth discussion of a result following this line of reasoning is beyond the scope of this section and a simpler approximation is used.

A collision between atoms of similar atomic weight produces a wide range of final velocities. This range extends from an inperceptible change for glancing angles to an exchange of velocities for head-on collisions. This is approximated by assuming that the velocity of each atom is thoroughly randomized. However, under the conditions of interest where there are relatively few Cs atoms in a higher concentration of buffer gas atoms, collisions between dissimilar atoms are more likely. The ratio of the momentum of the heavier Cs atoms to that of the lighter buffer gas atoms is

$$\frac{momentum_{Cs}}{momentum_{buffer}} = \sqrt{\frac{mass_{Cs}}{mass_{buffer}}} \quad . \tag{7.5}$$

The square-root relationship in momentum helps lighter collision partners to impart a significant momentum change to the Cs atom. The approximation used in the computer code, that the emitting Cs atom has a completely random velocity after collision with a buffer gas atom, becomes increasingly valid at higher temperatures and pressures since the collision rates are increased. Under these circumstances, multiple collisions are more likely and velocity randomization is assured. The randomizing approximation is certainly valid for high atomic weight buffer gases, such as krypton and xenon, at 84 and 131 amu. respectively, under all conditions.

Validation of Velocity Approximation

The conclusions drawn by Huber[45] reinforce the above assumptions on atomic emission. He concluded that in the case where (Doppler width) > > (natural width) > > (collisional width), the "frequency distribution of scattered light is narrowed in the forward and backward directions, and has the full absorption width for right-angle scattering." For forward scattering under these conditions the previous subsection states that the absorber's velocity in the direction of the incident photon is solely responsible for the Doppler shift of the incident light to the transition frequency. This defines the velocity in the forward direction precisely; the emission line in the forward direction is therefore centered at the initial excitation frequency and has a bandwidth equal to the Lorentzian characteristic width. The constraint on the relative widths of the natural and collisional contributions insures that the atom does not undergo a significant change in velocity. The emission width for right-angle scattering has added to it the full Doppler width since the velocity in the perpendicular direction is not constrained by the excitation frequency. An experiment to verify these results would have to be conducted in a vapor cell that was optically thin, meaning that reabsorption would be so unlikely that only one interaction could occur. Multiple interactions would produce a signal in the forward direction that was not solely derived from forward scattering and thus have a wider frequency distribution.

Flowchart used in Computer Modeling

Figure 7.2 is a flowchart based on the workings of the computer model. It covers only the processes involved in absorbing and re-emitting one photon.

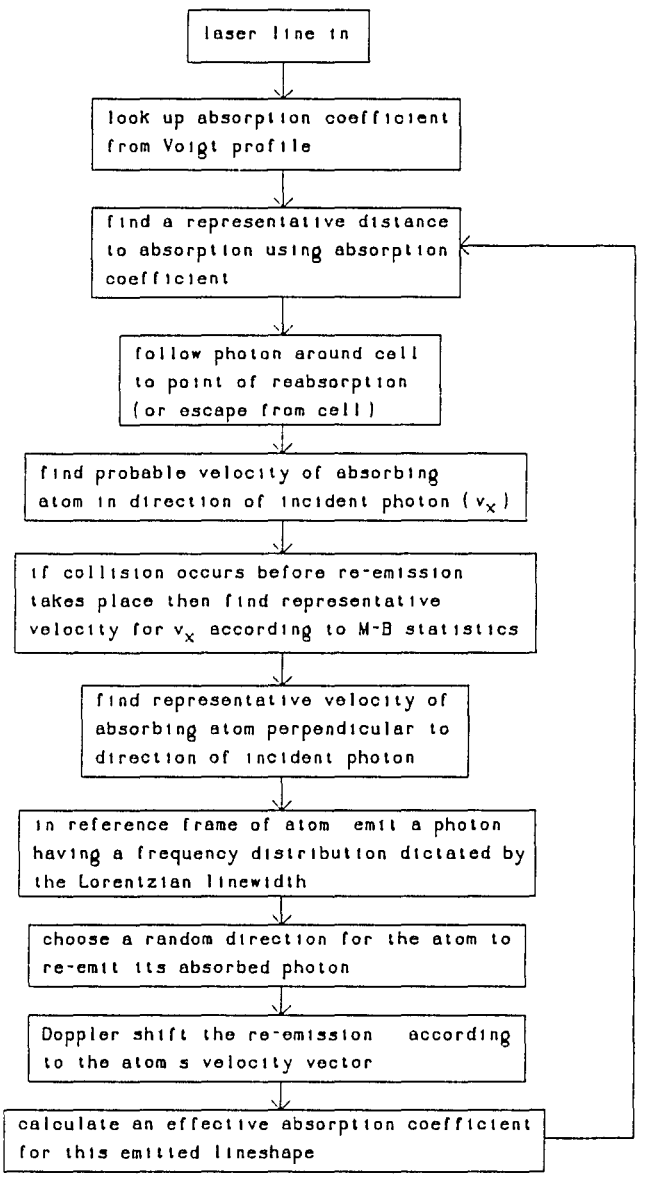

Figure 7.2. Flowchart for the simulation of absorption (emission) of radiation by a gas layer.

Section 8: Model Verification and ARF Performance

Two simple tests were performed to verify the correctness of the computer code generated according to the model just presented. In these tests the vapor was contained in a glass enclosure that is referred to hereon as a "cell". The cell had a dimension of 1cm in the direction of the blue signal light which was generated by an argon pumped, tunable ring dye laser which had a bandwidth of $\sim$200KHz. The first test measured the 455nm light, hereon denoted as "blue light", that passed through the cell with an attenuation that depended on temperature. The second test measured the conversion efficiency, η_c, defined as the ratio of the sum of 852 and 894nm "red" photons out to the 455nm "blue" input photons, which was also as a function of temperature.

The measurement of the amount of blue light that passed through the cell verified the magnitude of the absorption at line center and the Cs vapor density as functions of temperature. It therefore indicated that the convolution process was numerically correct since the numerical values of the individual Gaussian and Lorentzian functions were known to be correct. In the physical setup, shown in Figure 8.1, an aperture was placed on the output side of the cell that was just large enough to transmit the input laser signal without obstruction. This stopped essentially all of the blue light re-emitted into 4π steradians by the vapor. Cell temperature, (T_c), which determines the kinetics of the vapor, was stabilized by placing the cell in a rheostat-controlled oven. It is T_c that determined the kinetics of the vapor. The reservoir, a

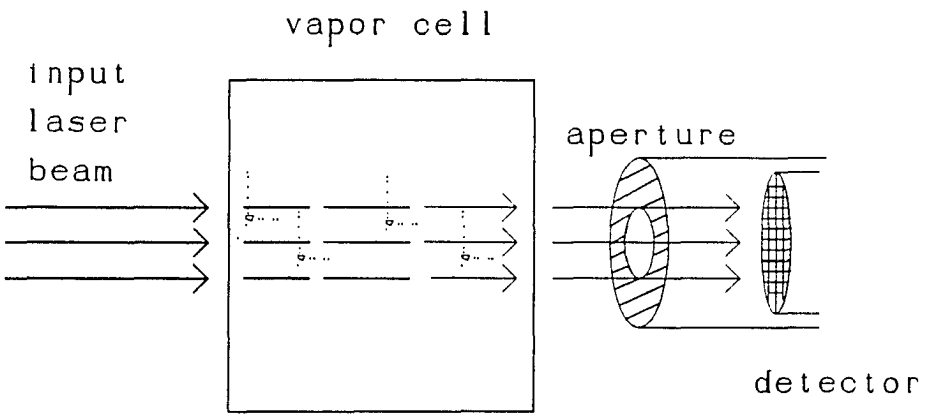

Figure 8.1. Setup for measuring vapor absorption at 455nm as a function of T_r.

small tube attached to the side of the cell that held the excess liquid Cs, was cooled slightly relative to T_c by a Peltier thermo-electric cooler to provide a preferential place for cesium to condense. This assured that condensing Cs did not occlude the input/output cell faces. This reservoir temperature (T_r) determined the equilibrium Cs vapor pressure, and therefore density, in the cell. Figure 8.2 shows the cell transmission as a function of T_r. The simulation curve assumed that $T_c = T_r + 5°C$. The error bars on the measured points were due to an uncertainty in the exact value of T_r, due to the attachment of the thermocouples to the Peltier cooler and the cell surface, not the reservoir. The lower endpoint of the error bars represents the reservoir temperature and the upper endpoint the cell body temperature. The true T_r was in between these two values. The data are in good agreement with prediction, within measurement uncertainty.

The second test compared the measured and calculated values of η_c as a function of T_r. The input and output walls of the cell were again uncoated but the side walls were given an opaque silver coating to confine the light and maximize η_c. Due to the restricted work area of the heating oven it proved difficult to couple light from the cell to the PMT detector in the end-coupled configuration, with the input and output walls opposite each other. We then tried a second orientation, with the output wall adjacent to the input wall, denoted as side-coupling. The test results normalized to the maximum of the theoretical curve are shown in Figure 8.3. The data points are shown here with a constant 7°C error bar in T_r although the actual bars typically ranged from

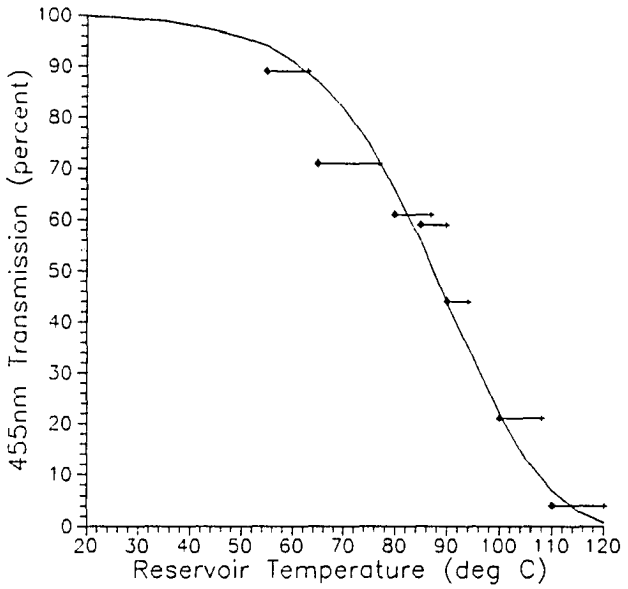

Figure 8.2. Transmission as a function of T_r for a 1x1x1cm cesium vapor cell.

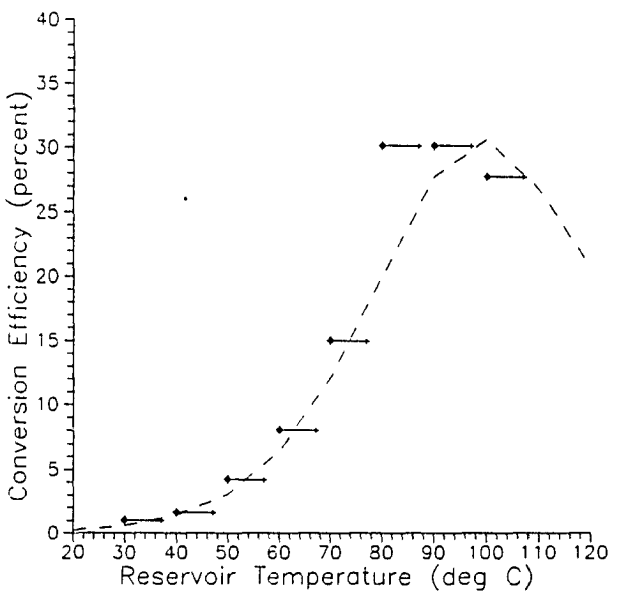

Figure 8.3. Conversion efficiency as a function of T_r for a side coupled 1x1x1cm cell.

4 to 12°C. The comparison was excellent for low T_r's (< 80°C) but some discrepancy occured at elevated T_r's. Without jumping ahead too far, this result could be due to trace impurities in the cell vapor which would decrease η_c by an amount proportional to the average number of collisions that an emitting atom encounters as the photon traverses the cell. This would have a pronounced effect at higher T_r's. If this hypothesis has merit, the data points are actually normalized at too high a value, which would bring the 80°C data point more into line with simulations and further drop the η_c seen above this T_r.

The performance of an ARF can be characterizedby its η_c and response time, τ_r. η_c is maximized by the systematic reduction of all losses. However, the parameters that are adjusted to reduce these losses usually increase system τ_r, which degrades response. The following section identifies the losses and discusses the tradeoffs made in response rate. The following subsections describe this tradeoff between η_c and τ_r.

Section 8.1 Loss Mechanisms

Since the processes of atomic absorption and emission are lossless in a pure vapor, the loss mechanism that underlies this particular temperature dependence of η_c has only two possible sources. Either the blue input or deep red output photons escape the cell undetected or are absorbed in collisions with an imperfectly reflecting surface. These pathways are explored below for the case of a glass cell having silvered side

walls and uncoated input and output faces.

A photon escapes the cell undetected if it exits through the input face since it will never reach the detector. Figure 8.4 graphically shows the simulation derived temperature dependence of the losses for a 1cm thick cell that is side-coupled. Since the vapor is optically thin at low temperatures due to the low Cs concentration, blue photons tend to pass through the cell, reflect off the opposing silvered wall, and exit through the input face. This source of loss remains even at high T_r's, where the Cs density is high and all the blue light is absorbed in the first few millimeters, since an atom in the excited 7p state can re-emit a blue photon toward the input window. The red photon loss increases with temperature since the red photons are first emitted closer to the input face. This loss is avoided if a SWP interference filter is added to this face. Blue photons may also exit through the output face if no LWP filter reflects them. These photons were not detected in our experiments because an absorption filter, which prevented false signals from occurring from surface scattering, kept these photons from reaching the detector. Another loss that vaguely fits under this category is the 7% insertion loss that is experienced as photons are reflected off the input window and never actually enter the cell.

The losses due to photon absorption at interfaces are reduced by careful selection of materials. The cell walls are very transparent since they are constructed from optical grade glass. Therefore the uncoated input and output walls have reflection properties

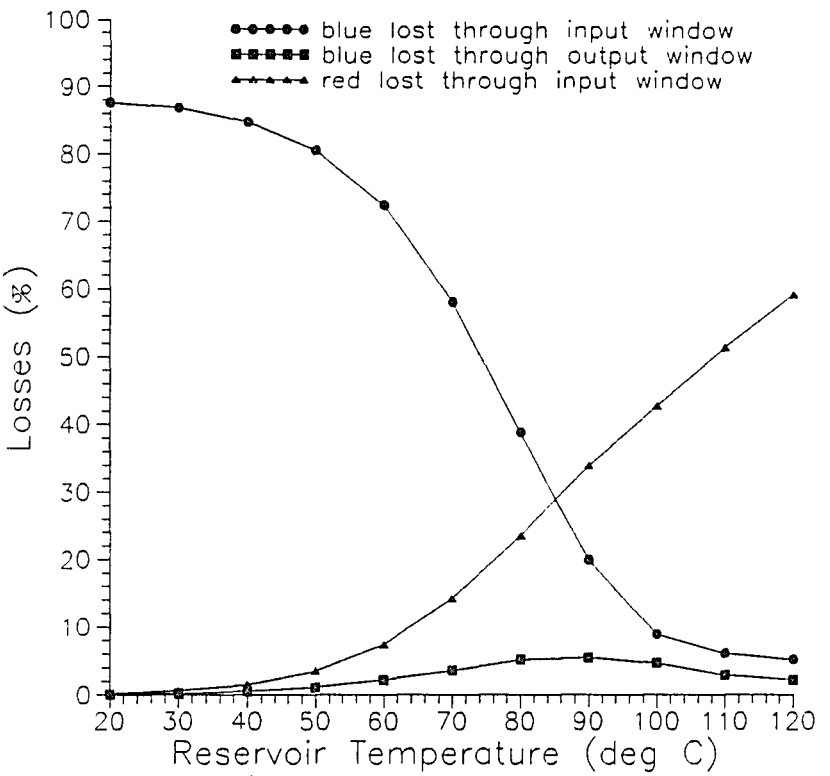

Figure 8.4. Simulated photon losses of a 1x1x1cm uncoated, side-coupled cesium cell.

that follow the Fresnel equations for a glass/air interface and have very low absorption. The remaining walls have an opaque silver layer deposited on their exteriors with a reflectance of over 96% at all angles. The average decrease in conversion efficiency due to the absorption at the silvered walls is minimal, between 3 and 5% over the entire temperature range.

Section 8.2: Additional Simulation Results

The response time, τ_r, of the ARF depends on two factors. The first is the rate at which one atom decays to its ground state, which is primarily determined by the natural lifetimes. However, this rate is increased by collisional broadening. The second factor is the number of times the input photon is absorbed and re-emitted, which depends on both the Cs concentration and the cell dimensions. The product of the rate and number of absorptions determines the response time of the system. Figure 8.5 shows the ARF's temporal response from a typical simulation having a delta-function input signal.

Since the Cs vapor density is known to have a strong temperature dependence, the pulse duration is expected to show a similar dependence. The response time, τ_r, defined as the average time delay between entering the cell as a blue photon and exiting through the output window as a red photon, was determined through simulation as a function of temperature. The results are displayed in Figure 8.6 alongside a plot of η_c for a 1cm cubic, end-coupled cell with 20 Torr neon buffer gas. The response time has

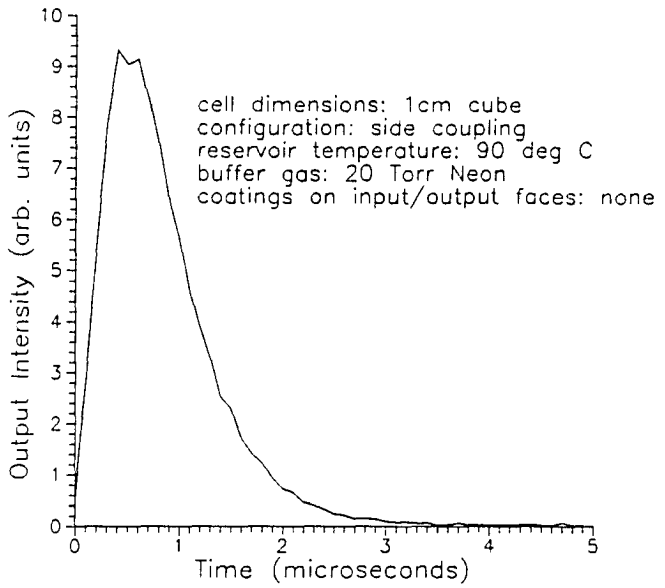

Figure 8.5. Temporal response of an ARF for an input applied at Time=0.

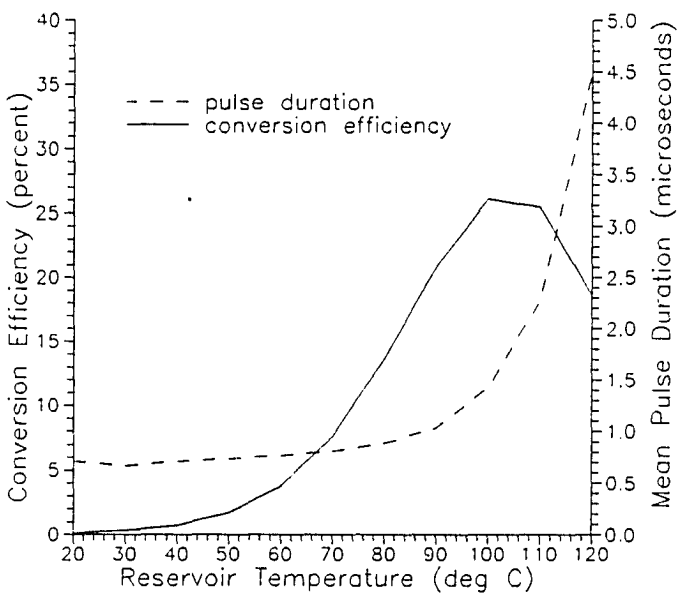

Figure 8.6. Response time and conversion efficiency of a cesium cell.

two effects. There is a delay that is nearly constant with temperature which is due to the radiative cascade from the 7p to 6p states. This delay is encountered by every output photon only once. The second is related to the number of absorption/emission cycles encountered by the photon leaving the 6p state. The time that the all photons spend in transit is $<0.01\%$ of the cascade time. The optimum tradeoff between η_c and τ_r for this particular cell appears to be in the range from 80 to 100°C.

Figure 8.7 shows the number of times that a red photon is absorbed and re-emitted for the same cell. This large number of interactions at high temperatures increases the τ_r and makes radiation trapping a dominant effect, changing the output lineshape, as will be shown later.

The comparison between the expected η_c's for the end-coupled and side-coupled cases is shown in Figure 8.8. At low temperatures, when the Cs vapor is optically thin, the side-coupled configuration is nearly twice as efficient as the end-coupled configuration. This occurs since the blue light gets two passes through the side-coupled cell before exiting versus a single pass for the end-coupled configuration. This is a direct consequence of having a mirrored side opposite the input window.

One also might wish to find the maximum η_c possible from a Cs ARF. A run was executed using perfectly reflecting silvered walls and ideal SWP/LWP filters, that is, filters with no absorption component. η_c and τ_r are presented in Figure 8.9. The

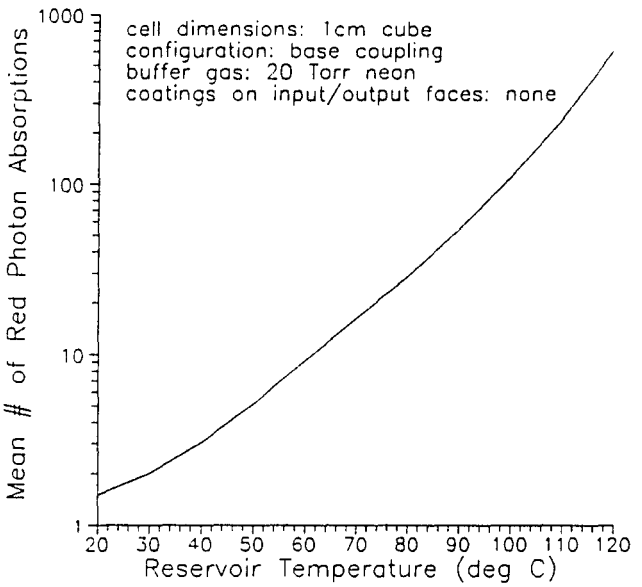

Figure 8.7. Mean number of red photon absorption/re-emission events for every 455nm input photon.

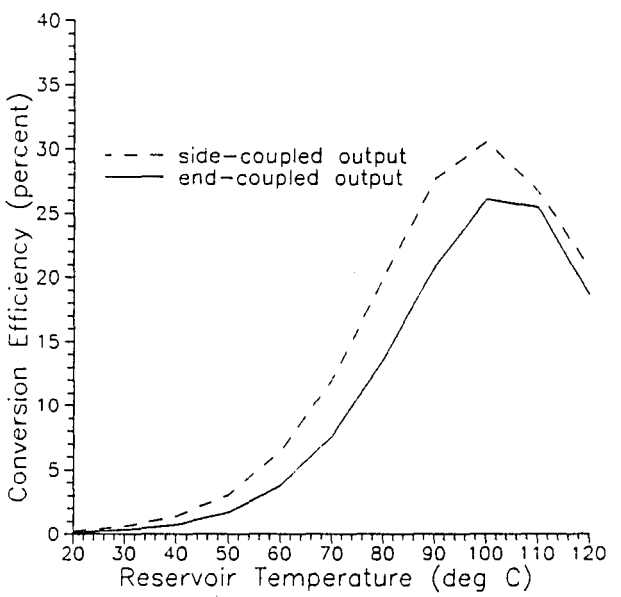

Figure 8.8. Output configuration comparison for a 1cm cubic cell.

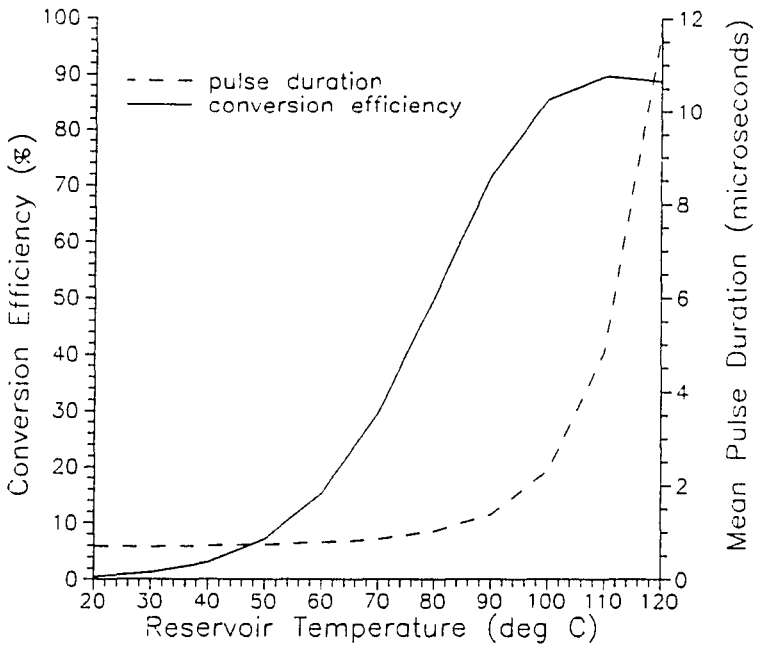

Figure 8.9. Performance of a cell having ideal (perfectly reflecting) walls.

extra confinement of the photons provided by these ideal surfaces increases τ_r at high temperatures by nearly a factor of three.

The output radiance profiles as a function of angle, shown in Figures 8.10 and 8.11, are important since they show the difference between the outputs of a side-coupled cell containing vapor that is optically thin and optically thick respectively. Figure 8.10, showing the optically thin case, resulted from a T_r of 20°C. It has superimposed on it the ideal isotropic radiance profile. The optically thick case, which has a Lambertian profile superimposed on it, was simulated using a T_r of 90°C and appears in Figure 8.11. Both simulation plots appear to approach the superimposed curves except for one notable exception. Since the emission from any point in the cell is more likely to exit the cell if it travels in a direction normal to the output window, and therefore has less chance of being reabsorbed, the lower angles have an increased rate of occurrence.

The mean exit angle is plotted as a function of T_r for a 1cm cubic cell in Figure 8.12 for both end- and side-coupled configurations. The cell has mirrored side walls and bare input/output surfaces. This figure shows that there is a significant change in the radiance pattern for the end-coupled case over the 20-120°C range of T_r. This must be considered if the efficiency of the collection optics from the output side to the detector is angle dependent, such as with the fiber optic coupler used in these

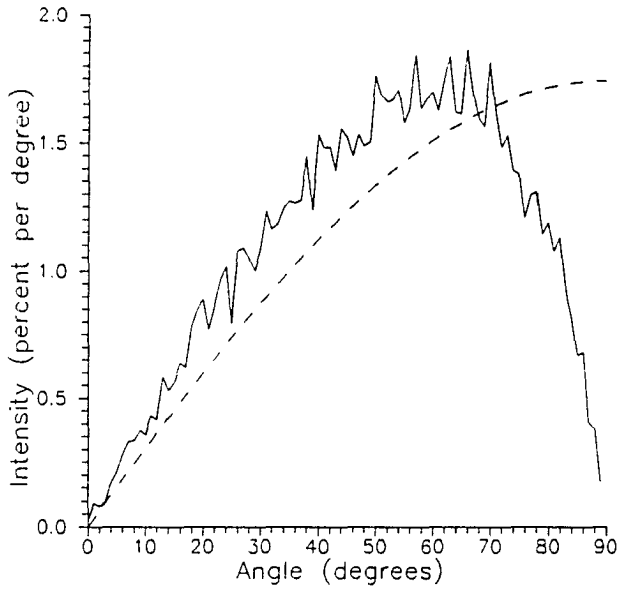

Figure 8.10. Output radiance profile for a cell having optically thin cesium vapor. Isotropic emission profile is the dashed line.

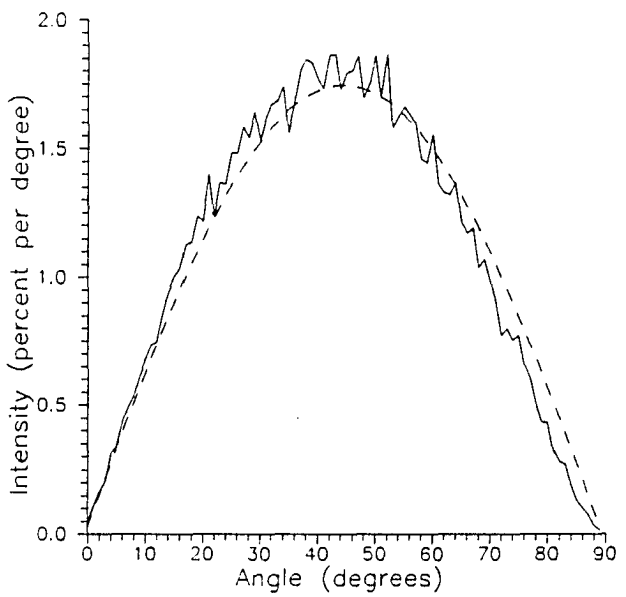

Figure 8.11. Output radiance profile for a cell having optically thick cesium vapor. Lambertian emission profile is the dashed line.

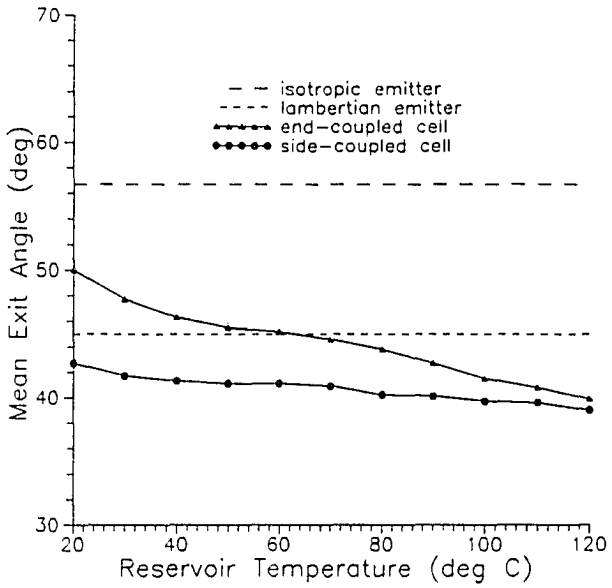

Figure 8.12. Mean exit angle for end- and side-coupled cells superimposed on the dashed values for Lambertian and isotropic sources.

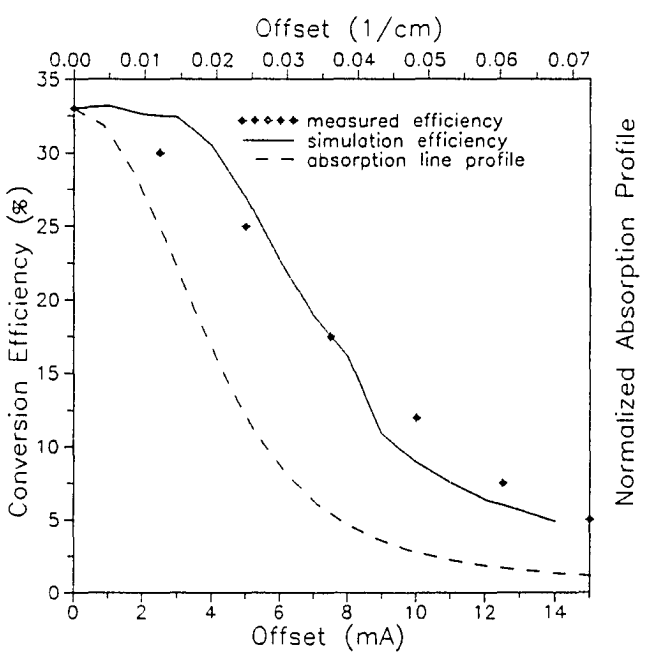

Figure 8.13. Cell conversion efficiency as a function of laser offset for T_r=90°C.

experiments. However, our experiments were conducted with side-coupled cells. Little change in detector coupling efficiency is therefore expected over the range of 80-120°C, and this is not a contributing factor to the early drop-off in efficiency as a function of temperature as seen in the experiment.

η_c as a function of laser offset wavelength, λ_{off}, depends strongly on T_r. The measured values of η_c for T_c=90°C appear in Figure 8.13. The simulation curve has been normalized to the measured η_c at zero offset and is in agreement with the data to within the statistical variation. The absorption profile, is shown for comparison of the FWHM of η_c and the absorptance, α. The Cs density is high enough at 90°C to absorb most of the light up to 4mÅ from line center, where the absorption is only one half its maximum value. This is not the case for low T_rs since the cell is optically thin at all values of offset. In this case, the conversion efficiency, which is limited by the number of blue photons absorbed, follows the absorptance profile.

At T_r's above 90°C, cells without a SWP filter on the input window experience a decrease in η_c due to the escape of red photons, as previously mentioned. By moving the laser wavelength slightly off resonance the mean photon penetration into the vapor is increased, placing the first fluorescence event further from the input window. This reduces the amount of red light lost via this route and increases efficiency. Figure 8.14 is a 3-D plot of η_c versus both temperature and offset. Note that the maximum η_c has moved from zero offset.

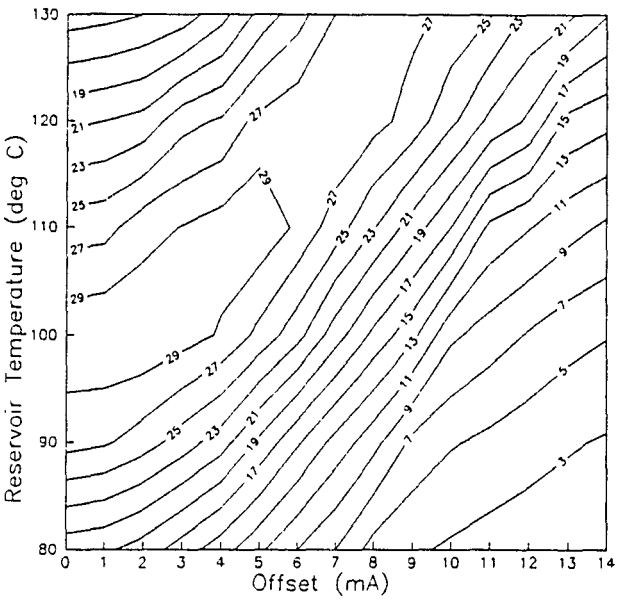

Figure 8.14. Contour plot of conversion efficiency (η_c) as a function of offset and temperature.

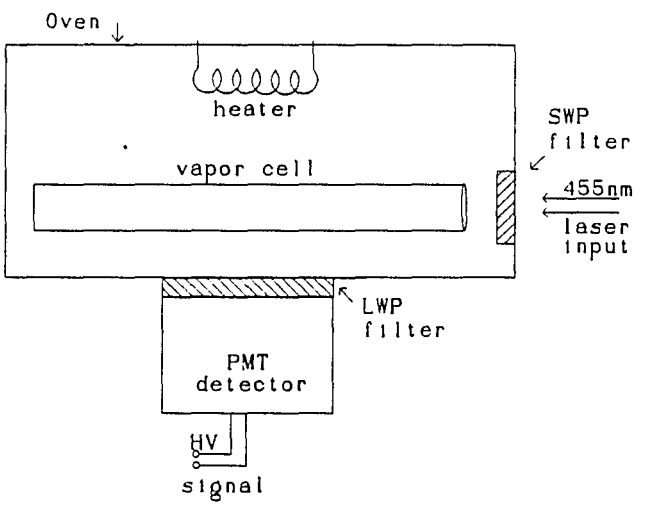

Figure 8.15. Experimental setup used by Marling et. al. to observe η_c as a function of offset.

This result was the probable source of confusion in early reports of η_k in Cs cells[46]. The peaks in η_c were originally thought to be centered about a pair or partially resolved hyperfine structure transitions separated by 20mÅ. An article[47] written in rebuttal to this conclusion pointed out that this "hyperfine" structure spacing was not in agreement with accepted literature values. No hypothesis was offered in explanation of Marling's results. A simulation of this experiment is ideal for analyzing these results, however, without knowing the precise laboratory setup exact numerical agreement is not expected. A diagram from Marling's paper is reproduced in Figure 8.15 showing a rough setup. Marling indicated that the cell was glass, side-coupled, and operated at 127°C. There was no mention of a buffer gas. A simulation was performed using this information and the resultant function of η_c versus offset for a 1cm cubic cell had a separation of the two maxima of 13mÅ, close to the 20mÅ measured value. The maxima separation increases with cell depth, and a slight underestimate of the experimental cell depth would account for this discrepancy.

Further explanations of ARF performance are offered after a brief discussion of radiation trapping and its effects on pulse stretching, output signal spectra, and conversion efficiency.

Section 9: Radiation Trapping

The purposes of this section are to define radiation trapping, or imprisonment, and to show its effect on ARF properties. Discussion is chronological, starting with an early approach of Compton and continuing with later advances by Kenty and Holstein. The effect of imprisonment on the emission lineshape and apparent lifetime of an excited state is stressed.

In a homogeneous gas, when an atom spontaneously emits in a transition to the ground state, the resulting photon interacts strongly with the surrounding medium. This occurs because most of the surrounding atoms are in the ground state, even for strongly irradiated gases, and all are capable of absorbing the emitted quanta, raising the surrounding atoms to the energy level initially excited in the first. If the absorption coefficient and the dimensions of the gas volume are large, the photon will undergo repeated absorption/emission events before it escapes the gas boundaries, and it is therefore called "trapped". The apparent lifetime of the excited state of the gas is greatly enhanced by this effect, and is estimated by the product of the number of absorptions and the excited state lifetime of an isolated atom.

Calculating the expected number of absorptions/emissions undergone by a photon in such a medium was first approached by K. Compton[1]. He believed this phenomenon had the characteristics of a three-dimensional random-walk problem

characteristic of Brownian motion. A problem of this nature is described by a diffusion equation,

$$\frac{\partial n}{\partial t} = D\,\nabla^2 n \quad , \tag{9.1}$$

where n is the density of excited states and D is the diffusion constant. By assuming that the absorption follows Beer's law,

$$p(x) = e^{-x/\sigma_{mfp}} \quad , \tag{9.2}$$

which defines the mean free path as $1/\sigma_{mfp}$. The diffusion coefficient is found to be

$$D = \frac{\sigma_{mfp}^{\,2}}{3\tau} \quad , \tag{9.3}$$

where τ is the excited state lifetime.

The weakness of this approach was its assumption that every emitted photon and every absorbing atom were identical. This assumption allowed for the easy calculation of a mean free path, but did not account for the frequency spread created by Doppler shifts or collisions. This frequency spread, combined with a frequency dependent absorption coefficient that affects σ_{mfp}, adds considerable complexity to the problem. An improved probability distribution on distance before absorption is therefore

$$p(x) \;\rightarrow\; p(x,\nu) = e^{-x/\sigma_{mfp}(\nu)} \quad . \tag{9.4}$$

The next notable advance in this problem was made by Kenty[2]. He applied a diffusion equation to solve the case of a purely Doppler-broadened lineshape, and found that for an infinite medium, the calculated diffusion coefficient was unbounded. As a way around this difficulty, he developed a method for determining an effective diffusion coefficient which was accurate to an order of magnitude and could predict results in good agreement with experiment over limited conditions.

A more comprehensive approach was offered by Holstein[3], who used the frequency dependent Beer's law (9.4) and Bayes' theorem to find $p(x)$.

$$p(x) = \int_{-\infty}^{\infty} p(x|\nu)\, p(\nu)\, d\nu \quad . \tag{9.5}$$

The conditional probability $p(x \mid \nu)$ is the probability of traversing a distance x given the emission frequency ν.

Holstein knew that all characteristics of an imprisoning medium were dependent on the vapor density, enclosure geometry and shape of the resonance line. He started with the case of an infinite slab of vapor that exhibited only Doppler broadening. With the incident radiation impinging normal to the plane of the slab he found the number of absorptions to be

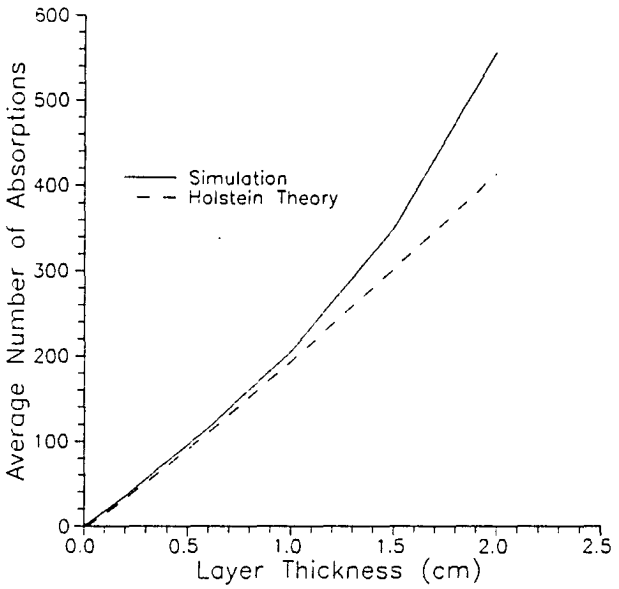

Figure 9.1. Average number of absorption events experienced in traversing a layer of Doppler-broadened gas. The temperature is 90 °C and the absorption at line center is 140 cm^{-1}.

$$absorption\ number = \frac{\alpha_o L \sqrt{\pi \log(\alpha_o L)}}{1.875} \tag{9.6}$$

where α_o is the absorption at line center, and L is the slab thickness. This is plotted in Figure 9.1 for the case where $\alpha_o = 140$ cm^{-1}. Of course, Holstein's relationship is not valid for distances such that $\alpha_o L < 1$, but also, the simulations show some deviation from the calculation at larger L's. There appears to be a second-order relationship with L on the number of absorptions. This quadratic result is more consistent with studies done on scattering atmospheres, which however, are not directly analogous to atomic scattering since the scattering coefficient of clouds is relatively frequency-independent.

For atomic vapors, frequency-dependent absorption leads to selective absorption closer to the line center. Photons near the line center are preferentially absorbed, and re-radiation covers the entire emission spectrum. Hence, the emission line spectrum of a volume of gas exhibiting imprisonment shows a dip at the line center, with a depth depth directly dependent on gas depth, as shown in Figures 9.2 and 9.3. This phenomenon is called self-absorption. When this occurs, the energy at line center slowly migrates to the emission wings where reabsorption is unlikely. The panels of Figure 9.3 display the data of Figure 9.2 in three dimensions. The FWHM of the emission line is graphed in Figure 9.4 to show how the steady-state lineshape evolves with L.

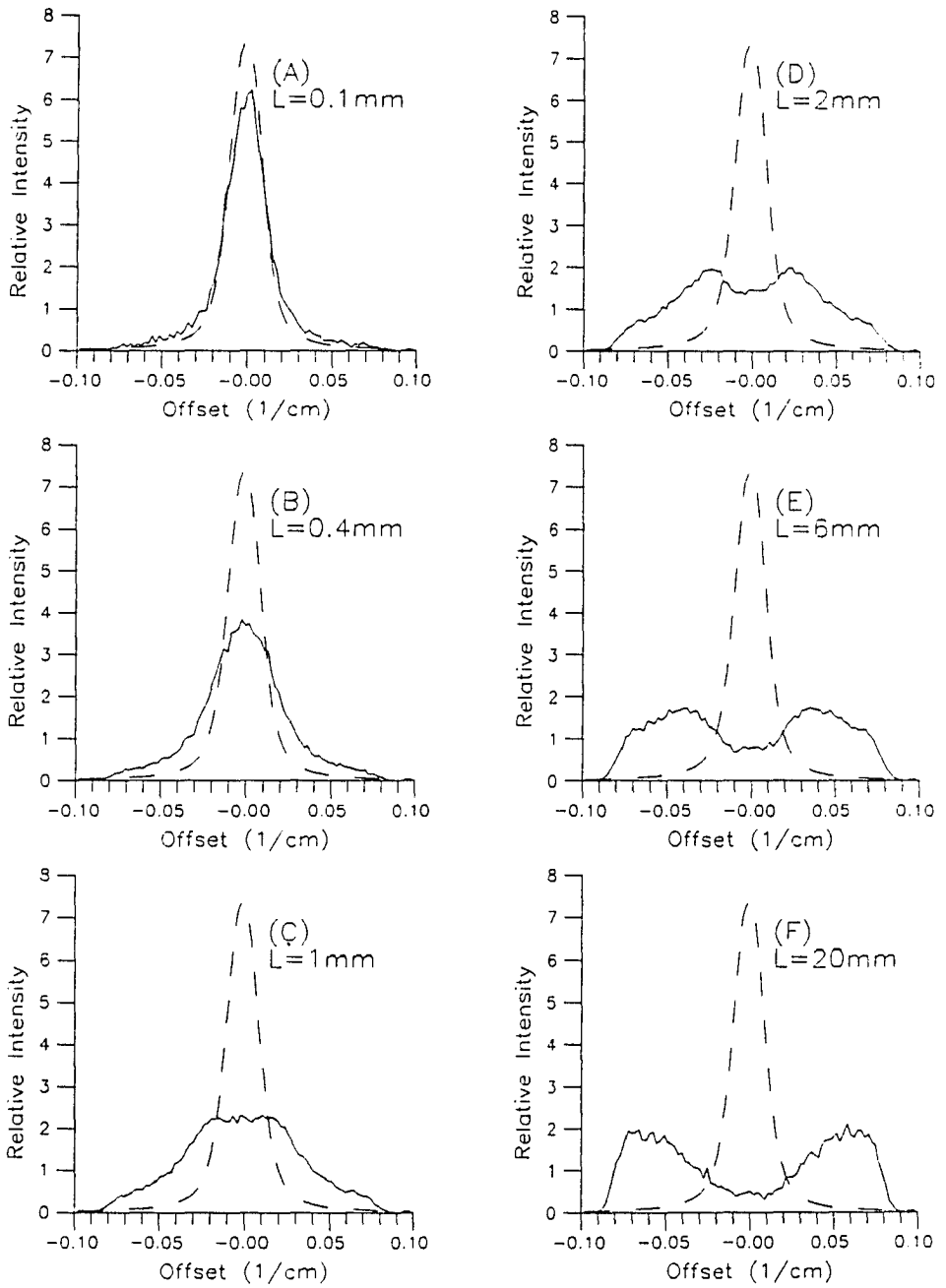

Figure 9.2. The evolution of the cumulative emission spectrum in the traversal of a layer (thickness L) of absorbing gas. The dotted curve is the emission/absorption line of an isolated atom.

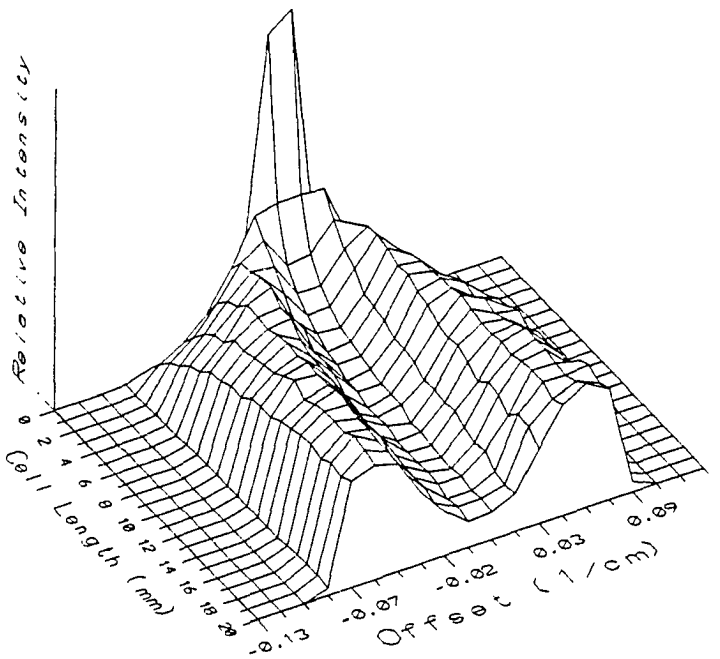

Figure 9.3. A 3-dimensional representation of the evolution of the cumulative emission spectrum.

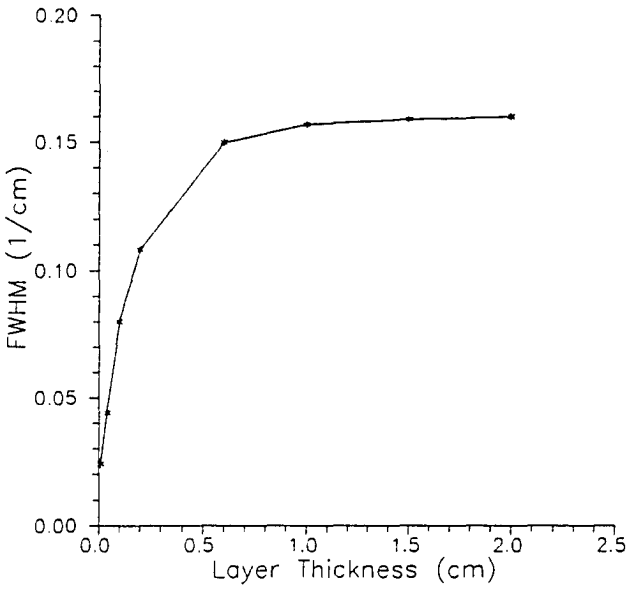

Figure 9.4. Evolution of the FWHM of the cumulative emission spectrum in the traversal of a layer of absorbing gas.

The comparison of simulations to theory indicates that further improvements in the model are necessary to understand the properties in the thick vapor region more fully. Agreement for thin vapor slabs is excellent, indicating again that the modeling presented here is accurate. However, slight deviations in the model from the exact physical phenomena occurring here are compounded when repeated over hundreds of interactions. Suggestions for improvement are offered in the Conclusions.

Section 10: Sources of Noise

Noise arises from several processes, all of which generate a signal at the detector when none was present. It is present when the SWP/LWP filters have incomplete blockage of non-resonant light and is created by the blackbody radiation from the cell itself. Certain LEOFs also suffer from energy pooling collisions that produce signal photons. This section serves to explain each of these processes and mention how some are avoided.

As mentioned before, interference filters (IFs) are mated with absorption filters to form the input/output SWP/LWP filters. The IFs are placed closest to the vapor cell and serve as dichroic filters. For example, the IF used in the SWP input filter reflects 852 and 894nm photons and transmits those at 455 and 459nm over a wide range of angles. The performance of these filters is maximized with regard to these select wavelengths with minimal effort expended in blocking other wavelengths. The absorption filters have the job of determining the filter rejection of non-resonant photons. Noise from the absorption filters arises in two forms, incomplete blockage of light and filter fluorescence. Both of these are minimized by careful selection of commercially available filters. Several low-fluorescence filters have recently become available.

Black-body (BB) radiation from the cell walls constitutes another source of

noise. The radiance, $L_\lambda(\lambda)$, generated by a surface at temperature T is described by the Planck radiation law, presented here as a function of wavelength.

$$L_\lambda(\lambda) = \frac{2hc^2}{\lambda^5} \frac{1}{e^{\frac{hc}{\lambda k_B T}} - 1} \qquad \left[\frac{W}{m^2 \cdot sr}\right] \tag{10.1}$$

It has a peak value as determined by the Wein displacement law.

$$\lambda_{L_{max}} \cdot T = \frac{1}{4.965} \frac{hc}{k_B} = 2.898 \cdot 10^{-3} \quad [meters \cdot K] \tag{10.2}$$

BB radiation creates a signal at the detector by two means. First, photons at 455/459nm simulate signal light and interact with the vapor, creating detectable red photons. This contribution is relatively small since absorption only occurs over the very narrow atomic absorption width. In the second, more likely scenario, BB photons in the near-IR spectrum pass unimpeded through the LWP absorption filter and are detected. Both types of BB noise are minimized by using surfaces with low emissivity and keeping these surfaces at the lowest possible temperature. Temperatures are determined by the cell size and the vapor pressure of the contained alkali metal. Cs and Rb cells, operating at $\sim 100°C$, have a slight advantage with this regard over Ca and Mg cells, which operate at $\sim 300°C$. The contribution of the BB sources to the total background noise is dependent on the detector sensitivity in the IR, since the radiance peaks at 7.7 and 5.0 μm respecitively for the above two temperatures. In addition to the wall contributions, the absorption filters themselves are radiation sources. Their emittance is reduced by thermal separation from the hotter vapor cell

combined with active cooling.

LEOFs have several noise sources in addition to the above. Since a large population of atoms exists in a prepared, excited state, collisions between excited atoms is common. By a phenomenon called energy pooling[1], a collision between two excited atoms leaves one in a lower excited or ground state and the second in a correspondingly higher excited state. This noise mechanism was observed in the Rb LEOF[2]. 420nm output photons, whose intensity was a function of the 795nm pump intensity, were generated in the absence of the 532nm signal light. The mechanism is described below. Active pumping populates the 5p state.

$$Rb_{ground}(5s) + h\nu_{pump} \rightarrow Rb^{*}(5p) \tag{10.3}$$

Collision of two excited state atoms then creates a highly excited atom.

$$Rb^{*}(5p) + Rb^{*}(5p) \rightarrow Rb_{ground}(5s) + Rb^{*}(5d) \tag{10.4}$$

Radiative cascade from the 5d state produces an output photon at 420nm.

$$Rb^{*}(5d) \rightarrow Rb^{*}(6p) + h\nu \tag{10.5}$$

$$Rb^{*}(6p) \rightarrow Rb_{ground}(5s) + h\nu_{420nm} \tag{10.6}$$

This also corresponds to one of the output photons generated after a 532nm signal photon is absorbed from the 5p state. In the case of Rb LEOFs, this problem is avoided by using an absorption filter to remove all wavelengths created by the decay of the excited 6p state. Energy pooling is also avoided by operating at lower

temperatures since this reduces collision rates by lowering both atom density and mean velocity. The tradeoff made by operating at lower temperatures is an increase in the mean absorption length and the size of the cell.

Energy pooling will not occur under the conditions that Cs ARFs are useful as detectors. First, the signal intensities required for using the Cs ARF as a detection device are very low. A comparable sodium cell that exhibited energy pooling required a signal intensity of 1-100 Watts/cm^2, many orders of magnitude beyond the expected operating range of the Cs ARF. Secondly, the state that exhibits the most radiation trapping, the lower 6p state, does not have a level at twice its excitation energy.

In addition to energy pooling, one must consider photoionization. Cs ARFs will not suffer from this effect if the collecting optics do not transmit ionizing radiation ($\lambda < 318$nm), which would ionize a ground state Cs atom. There is not a significant population in the excited 6p state to be photoionized under the constraint of weak signal intensity.

The photons created by the processes of energy pooling and photoionization constitute noise for instance in the Rb LEOF, creating a signal where none was present. However, if these processes were to occur in the Cs ARF, they would actually decrease the output signal. Although unlikely at low intensities[3], two atoms in the 7p state could undergo energy pooling, but the result would be that instead of getting two red

photons out, at most one would be generated. Energy pooling is possible only in the presence of blue signal, and the result is that the detector signal is reduced and the background noise is not increased.

Section 11: Results and Conclusion

The results of simulations have been compared throughout this dissertation with experimentally derived values. This section recapitulates these results from another perspective. First, a comparison is made with a previous model, one in which the atomic velocities were not accounted for in determining the emission distribution. We compare the curves of η_c vs. T_r, and η_c vs. offset frequency ($\Delta\nu$) in Figures 11.1 and 11.2 respectively. Next, we review the additional experiments performed to look at specific observable quantities, such as the 455nm absorption coefficient (α_{455}), and the red fluorescence pulse shape and duration. Following this, we examine less accessible model parameters for insight into optimum Cs cell dimensions and coatings. Lastly, we list areas of continuing interest.

The advances that were implemented in the process of improving the ARF simulation can be compared with the results from an earlier model. Two relationships were of concern in the early work, η_c vs. T_r and η_c vs. $\Delta\nu$. The older results are plotted alongside those of the present model and experimental results in Figures 11.1 and 11.2 respectively, with the curve of η_c vs. $\Delta\nu$ having a T_r=90°C. The improvement in the $\Delta\nu(T_r)$ results brings the simulation to within experimental error. The deviation of present model results from measured values in the η_c vs. T_r simulation is an improvement over the previous version but is not within experimental error. This point is covered at the end of this section.

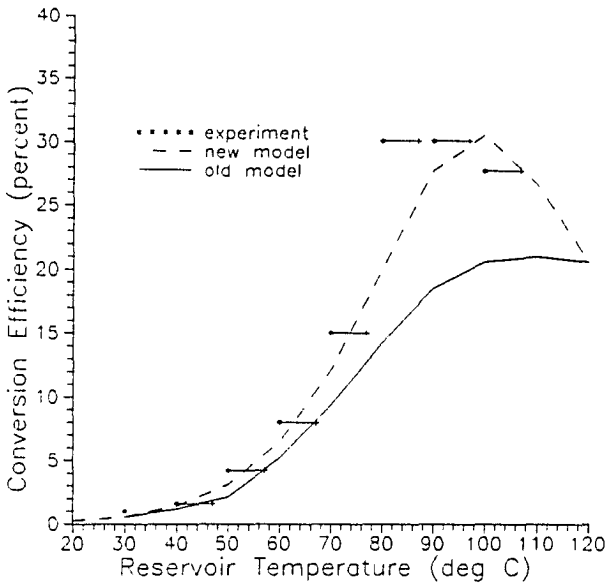

Figure 11.1. Improvements made in ARF simulations: η_c vs. T_r.

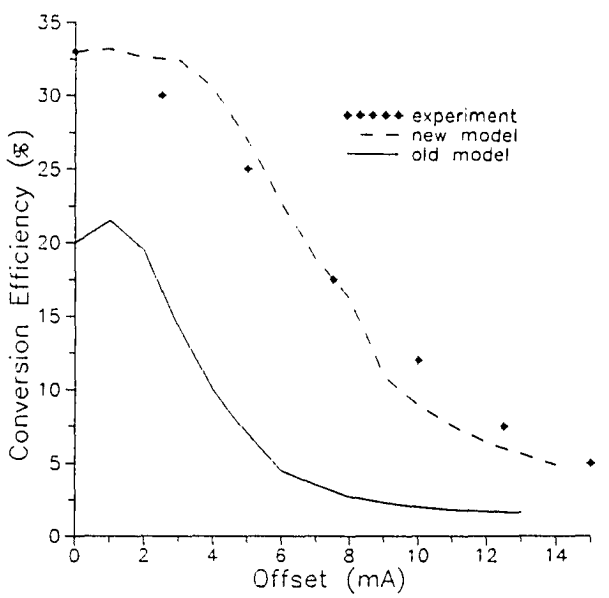

Figure 11.2. Improvements made in ARF simulations: η_c vs. $\Delta\nu$.

The major improvement made to the model correlates atom velocities with $\Delta\nu$, as measured from line center, of the input light. This generates the intuitive result of Huber that if Doppler broadening dominates over natural and collisional broadening, then forward and backward scattered light experiences line narrowing. Forward scattered light, if scattered only once, appears at the incident frequency; backward scattered light appears at twice the $\Delta\nu$ of the incident light but on the opposite side of line center. As reviewed in Figure 11.3, this occurs because in the purely Doppler-broadened case, the atomic velocity is exactly determined by the offset frequency, as the Doppler-shifted incident photon must appear exactly on line center. If a small amount of natural broadening is present, as in any experiment, then the forward and backward scattering linewidths are comparable to the natural width.

Additional experiments addressed two other parameters. The first confirmed the degree of absorption of 455nm light, which is proportional to the product of the Cs density and an analytically derived absorption lineshape maximum found through the Einstein coefficients. The model gave the correct results for the 455nm transmission vs. T_r curve, confirming that these variables were appropriately integrated. The confirmation of the red 852nm and 894nm light absorption was obtained by observing the output pulse shape and duration. The former is very dependent on the red absorption characteristics since several thousand red absorption/emission events can occur if the vapor is optically thick and the cell sufficiently long.

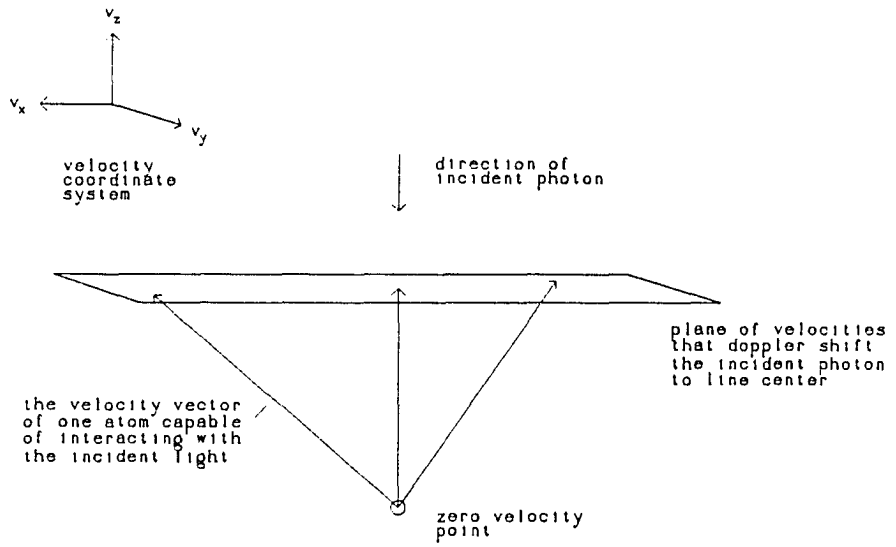

Figure 11.3. Line narrowing from a single absorption/emission event which re-radiates in the forward or backward direction. The direction of the incident photon and its $\Delta\nu$ determines exactly the atomic velocity parallel to the incident photon (v_z). Emission parallel to v_z has a width determined by the natural width and a line center determined by the Doppler shift. Emission perpendicular to v_z again has a natural linewidth associated with spontaneous decay, but the Doppler shift is averaged over the entire v_x-v_y velocity plane, which is the entire M-B distribution of velocities, resulting in the full Voigt profile for the emission line width.

There were several parameters which would be difficult to measure, so the model was used to estimate this information. The 455nm and 852/894nm photon losses through the input and output windows were simulated to find a good combination of cell parameters to optimize cell performance. These losses explained why the curve of η_c vs. T_r had its particular shape. The dominant losses were the blue losses at $T_r < 80°C$ and red losses at $T_r > 90°C$, producing a maximum η_c at about 85°C.

We found that the coating of the input window was very important. Ideally it should transmit the blue photons and reflect the red photons over all angles. A study of the exit angles at both wavelength intervals found the range of angles involved. The red photon exit angle distribution was found to go from nearly isotropic to nearly Lambertian as the cell temperature rose from 20 to 120°C. This information served as input for improved filter design as well as confirmation that the output fiber coupling from the cell to the detector was not dependent on temperature, or output profile. Indeed, we found that the output aperture coating had less impact on performance than that on the input aperture.

The simulations performed at various T_r's as a function of $\Delta\nu$ explained the apparent "hyperfine splitting" that was reported by Marling and questioned later by Flusberg. Although the exact experiment was not known, a study of a similar setup was performed and an apparent "doublet" was observed. This was not due to hyperfine splitting but to the disproportionately high red photon losses from the input aperture

present at low $\Delta\nu$ values.

At this point, our major discontent with the model results is the low T_r falloff of efficiency, η_c. There are two ways to solve this problem. First, there may be trace impurities in the buffer gas. Cesium does react with many elements, so any of the unreactive species must be considered as a source for collisional de-excitation. This could be experimentally tested by starting with a cell containing only cesium and slowly adding buffer gas. There should be a dependence on the density of impurity atoms that relates directly to the decrease in efficiency through the number of absorption/emission events. The second possible mechanism for the loss in efficiency is collisional de-excitation with diatomic, or molecular, cesium. This source can never be removed since diatomic cesium is always present and in equilibrium with monatomic cesium. This second possibility can not be determined by experiment, but only simulated. It could be incorporated as a T_r dependent density of absorbing collisional partners.

The difference between the two types of de-excitation hinges on the fact that the impurity density does not change as the temperature changes, whereas the diatomic cesium density grows exponentially with T_r. The final determination of which is dominant is made more difficult by concurrent exponential increase in the average number of collisions as T_r rises.

Appendix A

This appendix is a condensed tutorial covering Monte Carlo methods and the use of transformations as outlined by Frieden[1]. It explains the difference between the Monte Carlo and analytical approaches to a statistical problem. It also explains the concept and derivation of transformations and shows several examples.

The analytical approach to solving statistical problems is instructive when used to solve elementary textbook problems. In such a case one is typically given the probability law for an input variable and asked for the output probability law. For example if one is given the probability of the E-field values for an electromagnetic wave, the probability law for the intensity may be found. The transformation, an equation relating the input and output variables, of the E-field (random variable x) to intensity (random variable y) is of the familiar form

$$y=x^2 \tag{A.1}$$

This type of problem is easy to solve using the following approach.

The transformation

$$y=f(x) \tag{A.2}$$

in this case is already known. For a given input (x) the output (y) may be calculated. The inversion of this transformation is represented as

$$x=f^{-1}(y) \tag{A.3}$$

The above example has two roots, or two values of x for each y-value. Figure (A.1) is a graphical representation of this case. The event that occurs in the intervals dx_1 or dx_2 is identical to and is directly mapped into the event occurring in the interval dy by the chosen transformation f(x). Thus the probability of such an x-event occurring in the regions dx_1 or dx_2 is the same as that event occurring in dy. Expressed mathematically this becomes

$$p_Y(y)dy=\sum_i p_X(x)|_{x=x_i}dx \tag{A.4}$$

where the subscripts X and Y denote the particular laws in question. Substituting (A.3) into (A.4) produces

$$p_Y(y)=\sum_i \frac{p_X(f^{-1}(y))}{|\frac{dy}{dx}|}|_{x=x_i} \tag{A.5}$$

which is the formula for the desired probability law. Applying this to our example, if it is known that the E-field probability were uniform over the domain $0<x<1$ then the calculated probability on intensity would be

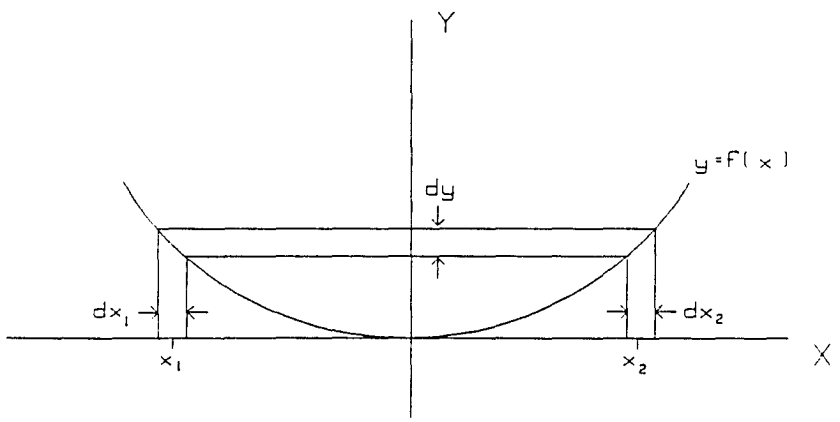

Figure A.1. Diagram for calculating a transform of a general function.

$$p_Y(y)=\frac{1}{2\sqrt{y}} \tag{A.6}$$

over the range $0<y<1$.

Performing the above calculations is not a demanding task, so why resort to numerical methods when an analytical result is obtainable? Simply stated, most real world problems are more complex than the example above, involving several physical processes and their corresponding probability laws. Consider the case of the absorption of photons by an atomic vapor that is enclosed by six walls, each having its own reflection properties (the reader is assured that this is a coincidental choice). This problem involves a negative exponential law for distance traveled before absorption, a uniform law for the isotropic re-emission angle for the continuing photon, a Gaussian distribution and a Lorentzian distribution for the re-emission frequency due to the Doppler shift and natural line broadening respectively. In addition the intensity of the light ray being traced through the vapor is attenuated by imperfect reflections from the wall depending on the angle of incidence. Obtaining an analytical result is at best impractical for real-life cases such as this.

But the real complication occurs because the physical processes occur in a sequence, with the input to one process depending on the output of the preceeding process. The ordering of the processes themselves varies depending on the preceeding outcomes. This is illustrated by considering the random value of the distance traveled

before reabsorption. A short distance will more likely be traversed without a wall collision than a longer distance. Thus the light traveling the shorter distance will not have to be weighted by the intensity loss on encountering a wall. This presents a problem because an analytical solution is dependent on the sequence of the processes. A solution would have to be calculated for every combination of sequences. When this occurs, it is not possible to find an analytical result and one turns to computer simulations using the Monte Carlo method.

The Monte Carlo method is based on the law of large numbers. This law states that the probability of a given event is equal to the frequency of occurrance of that event for very large trial sizes. So by constructing or simulating typical outputs of the system an estimate on the probability of an event occurring within a chosen interval $\beta < y < \beta + dy$ is found by observing the frequency with which events fall in this interval for discrete values of β. These typical outputs are constructed by sequentially progressing through the system, changing parameters that are affected by each particular physical process and assigning these parameters values that are typical of the probability law associated with such processes.

The only task remaining is to generate numbers that obey the various probability laws. As a rule computers are only equipped with a function call that will generate uniformly distributed random variables over the interval $0 < x < 1$. In Turbo Pascal[2] this function is called RANDOM. The random number generator provided by this as

well as most other languages has undesirable correlations. Better suited algorithms are available[3] and were used in the modeling. However, a transformation must be found to generate the other various laws using the the users choice of RANDOM variable generator for input.

The general procedure for finding a transformation is as follows. A unique root transformation is sought since it is demanded that only one output value be produced with each input value. In this case (A.4) simplifies to

$$p_Y(y')dy' = p_X(x')dx' \tag{A.7}$$

Since y is a function of x we observe that

$$F_Y(y) \equiv \int_{-\infty}^{y} p_Y(y')dy' = \int_{-\infty}^{f^{-1}(y)} p_X(x')dx' \equiv F_X(x) \tag{A.8}$$

which is the cumulative probability law {F(x or y)} for both distributions. If y is the uniform RANDOM output variable, then

$$y = \int_{-\infty}^{x} p_X(x')dx' = F_X(x) \tag{A.9}$$

This by definition is a single valued expression and is inverted to find the proper transformed value x.

$$x=F_X^{-1}(y) \tag{A.10}$$

This procedure will now be applied to find transformations that provide output according to Lorentzian, Gaussian, exponential and uniform solid angle probability laws.

A Lorentzian distribution has the form of

$$p_X(x)=\frac{1}{\pi}\frac{a}{a^2+x^2} \tag{A.11}$$

being charactorized by the constant a, for which it has a FWHM$=2a$. The transformation for a variable x that follows this law is

$$x=a\tan[\pi(y-\frac{1}{2})] \tag{A.12}$$

Calculating the transformation for a Gaussian distribution

$$p_X(x)=\frac{1}{\sqrt{2\pi\sigma^2}}e^{-\frac{x^2}{2\sigma^2}} \tag{A.13}$$

is somewhat perplexing because its cumulative distribution is an error function (abbreviated erf)

$$y=\frac{1}{2}erf\left(\frac{x}{\sigma\sqrt{2}}\right)+\frac{1}{2} \tag{A.14}$$

for which the error function is of the form

$$erf(z)=2\sqrt{\pi}\int_0^z e^{-t^2}dt \tag{A.15}$$

The Gaussian distribution has a FWHM=$\sigma(8\ln(2))^{1/2}$. The error function is not integrable. Its values are only available in tabular form and are only calculated through numerical integration. Thus analytic inversion of this function to solve for x is not possible. Inversion is possible only by numerically integrating the Gaussian and creating a table. A simple method for doing this is to record the x-value at which the cumulative probability is equal to increments of one percent. The Gaussian distributed variable is then found by linearly mapping the RANDOM variable to the previously chosen increment and reading the corresponding x-value.

The negative exponential law is of the form

$$p_X(x)=\frac{1}{a}e^{-\frac{x}{a}} \tag{A.16}$$

has the width determining parameter a, for which it has a FWHM=$a2\ln(2)$ and a variance of $\sigma^2=a^2$. The transformation of this law is

$$x=-\frac{\ln(y)}{a} \tag{A.17}$$

The final distribution that is of concern is the uniform distribution of direction that spans 4π steradians. In this case we desire a 3-dimensional vector (x_1, x_2, x_3) that has unit length, as shown in Figure (A.2). x_3 is arbitrarily selected as the first component to be calculated. A vector that has an angle of φ relative to the x_1 axis will have a probability of

$$p_{X_3}(x_3)dx_3=\frac{1}{2}\sin(\varphi)d\varphi \tag{A.18}$$

Using the transformation from x_3 to φ,

$$\varphi=\cos^{-1}(x_3) \tag{A.19}$$

we find that the probability on x_3 is a constant.

$$\therefore \quad p_{X_3}(x_3)dx_3=\frac{1}{2}dx_3 \tag{A.20}$$

The transformation giving the first vector component is

$$x_3=2(y-\frac{1}{2}) \tag{A.21}$$

The remaining two components add vectorally to give a unit length vector.

$$x_1=\sin(\varphi)\cos(RANDOM*2\pi) \tag{A.22}$$

$$x_2 = \sin(\varphi)\sin(RANDOM*2\pi) \tag{A.23}$$

where the same RANDOM variable is used in both equations.

In closing a remark should be made about the precision associated with the estimates of a probability found using the Monte Carlo method. As stated before the estimate approaches the actual probability as the number of trials increases. Since an infinite number of trials requires a serious amount of computer time, a finite number of trials that still gives the desired precision must be selected. The RMS error (ε) is

$$e_{rms} = \sqrt{\frac{p(1-p)}{N}} \tag{A.24}$$

where N is the number of trials and p is the frequency of occurrance (the estimate on the probability). The relative error is then

$$e_{rel} = \frac{e_{rms}}{p} \tag{A.25}$$

For example, if the frequency of occurrance is 20%, and 10% relative error were specified then it would require

$$N = \frac{1-p}{e_{rel}^2 p} = \frac{1-0.2}{(0.1)^2(0.2)} = 400 \tag{A.26}$$

for the trial size. The number of trials needed for a given precision can be reduced by increasing the interval size since the probability of an event occurring in that interval is increased. However, it is then difficult to make conclusive statements about the

probability at any specific region over this interval.

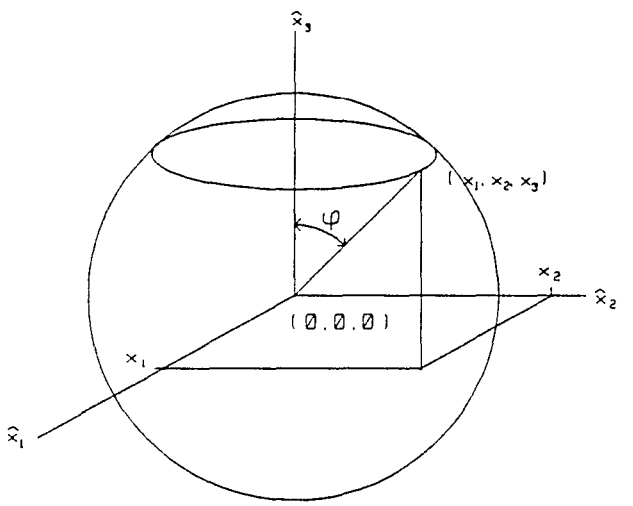

Figure A.2. Unit sphere relating angle with absolute coordinates.

REFERENCES

1. J.B. Marling, J. Nilsen, L.C. West and L.L. Wood, J. Appl. Phys. **50**, 610(1979).

2. T.M. Shay and Y.C. Chung, in Digest of Conference on Lasers and Electro-Optics (Washington D.C.: Optical Society of America, 1987), p.64.

3. Marling et. al., p.610.

4. J.A. Gelbwachs, C.F. Klein and J.E. Wessel, in Proceedings of Ninth Internationsl Laser Radar Conference (Institute of Atmospheric Physics, Munich, 1979), p.36.

5. H. Shimizu, S.A. Lee and C.Y. She, Appl. Opt. **22**, 1373(1983).

6. F.J. Lehnamm, S.A. Lee and C.Y. She, Opt. Lett. **11**, 563(1986).

7. J.A. Gelbwachs and J.E. Wessel, IEEE Trans. Electron. Dev. **ED-27**, 99(1980).

8. J.A. Gelbwachs, Opt. Lett **15**, 236(1990).

9. Marling et. al., p.610.

10. J.A. Gelbwachs, in Laser Spectroscopy VIII, W. Persson and S. Svanberg, eds. (Berlin: Springer-Verlag, 1987) p.409.

11. J.A. Gelbwachs, C.F. Klein and J.E. Wessel, IEEE J. Quant. Electron. **QE-14**, 77(1978).

12. M. Minden and H. Bruesselbach, Opt. Lett. **15**, 384(1990).

13. C.S. Liu, P.J. Chantry and C.L. Chen, Proc. Soc. Photo-Opt. Instrum. Eng. **709** (1986).

14. J.B. Marling, J. Nilsen, L.C. West and L.L. Wood, J. Appl. Phys. **50**, 610(1979).

15. F.A. Jenkins and H.E. White, Fundamentals of Optics, 4th ed. (New York: McGraw-Hill Book Co, 1976), appendix V.

16. A.E. Siegman, Lasers (Mill Valley CA: University Science Books, 1986), p.126.

17. P.W. Milonni and J.H. Eberly, Lasers ed. Robert Gray (New York: John Wiley and Sons, 1988), p.224.

18. A.N. Nesmeyanov, Vapor Pressure of the Chemical Elements (New York: Elsevier Publ. Co., 1963), p.146.

19. American Institute of Physics, American Institute of Physics Handbood, ed. Dwight E. Gray (New York: Colonial Press Inc., 1972), p.4-315.

20. A.R. Striganov and N.S. Svertitskii, Tables of Spectral Lines of Neutral and Ionized Atoms (New York: Plenum, 1968), p.45.

21. K.H. Weber, Phys. Rev. A **35**, 4650(1987).

22. Ibid.

23. P.F.A. Klinkenberg, Rev. Mod. Phys. **24**, 63(1952).

24. H. Kopfermann, Nuclear Moments (New York: Acacemic Press, 1958), p.15.

25. H. Casimir, Teylors Tweede Genootshap **11** (1936).

26. E. Arimondo, M. Inguscio and P. Violino, Rev. Mod. Phys. **49**, 31(1977).

27. M. Ortiz, J. Quant. Spect. Radiat. Transfer **26**, 107(1981).

28. B.N. Chichov and V.P. Shevelko, Phys. Scr. **23**, 1055(1981).

29. B.L. Wexler, R. Burnham and W.L. Nikolai, The Cesium Atomic Resonance Filter (Washington, D.C.: Naval Research Laboratory 1980).

30. J. Merek, J. Phys. B **10**, 1325(1977).

31. H.A. Lorentz, Proc. Roy. Acad. Amsterdam **8**, 591(1906).

32. E. Lindholm, Ark. Mat. Astron. Fus. **32A**, 17(1945).

33. H.M. Foley, Phys. Rev. **69**, 616(1946).

34. J.F. Keilkopf, J. Phys. B **9**, 1601(1976).

35. J. Szudy and W.E. Baylis, J. Quant. Spectrosc. Radiat. Transfer **15**, 641(1975).

36. J. Szudy, J. Quant Spectrosc. Radiat. Transfer **17**, 269(1977).

37. R.E. Walkup, A. Spielfiedel and D.E. Pritchard, Phys. Rev. Lett. **45**, 986(1980).

38. N. Allard and J. Keilkopf, Rev. Mod. Phys. **54**, 1163(1982).

39. Siegman, p.128.

40. N. Allard and J. Keilkopf, Rev. Mod. Phys. **54**, 1163(1982).

41. B.R. Freiden, Probability, Statistical Optics, and Data Testing (New York: Springer-Verlag 1983), p.38.

42. Milonni, p.102.

43. P.E. Toschek and W. Neuhauser, JOSA B **6**, 2220(1989).

44. A.L. Wells and R.J. Cook, Phys. Rev. A **41**, 3916(1990).

45. D.L. Huber, Phys. Rev. **178**, 93(1969).

46. Marling et. al., p.610.

47. A. Flusberg, J. Appl. Phys. **54**, 6036(1983).

48. K. Compton, Phys. Rev. **20**, 283(1922).

49. C. Kenty, Phys. Rev. **42**, 823(1932).

50. T. Holstein, Phys. Rev. **72**, 1212(1947).

51. A. Kopystynska, Phys. Rep. **92**, 136(1982).

52. M. Minden and H. Brusselbach, Opt. Lett. **15**, 384(1990).

53. J. Huennekens, Z. Wu and T.G. Walker, Phys. Rev. A **31**, 196(1985).

54. Frieden, p.99.

55. copyright of Borland Software Inc.

56. W.H. Press, B.P. Flannery, S.A. Teukolsky and W.T. Vetterling, Numerical Recipes (New York: Cambridge University Press, 1990), p.191.